



## Original Paper

# Experimental investigation of dynamic characteristics of leaching tubing for solution mining of salt cavern carbon and energy storage

Yin-Ping Li <sup>a, d</sup>, Xin-Bo Ge <sup>b, c, \*</sup>, Xi-Lin Shi <sup>a, d</sup>, Hong-Ling Ma <sup>a, d</sup>

<sup>a</sup> State Key Laboratory of Geomechanics and Geotechnical Engineering, Institute of Rock and Soil Mechanics, Chinese Academy of Sciences, Wuhan, 430071, Hubei, China

<sup>b</sup> College of Energy and Mining Engineering, Shandong University of Science and Technology, Qingdao, 266590, Shandong, China

<sup>c</sup> State Key Laboratory of Mining Disaster Prevention and Control Co-founded by Shandong Province and the Ministry of Science and Technology, Shandong University of Science and Technology, Qingdao, 266590, Shandong, China

<sup>d</sup> University of Chinese Academy of Sciences, Beijing, 100049, China



## ARTICLE INFO

## Article history:

Received 7 April 2023

Received in revised form

16 June 2024

Accepted 24 June 2024

Available online 26 June 2024

Edited by Jia-Jia Fei and Min Li

## Keywords:

Salt cavern storage

Solution mining

Leaching tubing

Experimental investigation

Flutter instability

## ABSTRACT

Salt caverns are extensively utilized for storing various substances such as fossil energy, hydrogen, compressed air, nuclear waste, and industrial solid waste. In China, when the salt cavern is leached through single-well water solution mining with oil as a cushion, engineering challenges arise with the leaching tubing, leading to issues like damage and instability. These problems significantly hinder the progress of cavern construction and the control of cavern shape. The primary cause of this is the flow-induced vibration instability of leaching tubing within a confined space, which results in severe bending or damage to the tubing. This study presents a model experimental investigation on the dynamic characteristics of leaching tubing using a self-developed liquid-solid coupling physical model experiment apparatus. The experiment utilizes a silicone-rubber pipe (SRP) and a polycarbonate pipe (PCP) to examine the effects of various factors on the dynamic stability of cantilevered pipes conveying fluid. These factors include external space constraint, flexural rigidity, medium outside the pipe, over-hanging length, and end conditions. The experiments reveal four dynamic response phenomena: water hammer, static buckling, chaotic motion, and flutter instability. The study further demonstrates that the length of the external space constraint has a direct impact on the flutter critical flow velocity of the cantilevered pipe conveying fluid. Additionally, the flutter critical flow velocity is influenced by the end conditions and different external media.

© 2024 The Authors. Publishing services by Elsevier B.V. on behalf of KeAi Communications Co. Ltd. This is an open access article under the CC BY-NC-ND license (<http://creativecommons.org/licenses/by-nc-nd/4.0/>).

## 1. Introduction

The energy security situation in China is currently grim, with a high dependence on foreign oil and natural gas in the past two years (Shi et al., 2023; Yang et al., 2023). Especially, the issue of “gas hunger” has emerged multiple times in recent years (Chen et al., 2020a, 2021; Feng et al., 2023), emphasizing the urgent need for large-scale energy storage. Due to the shortage of energy reserves (Chen et al., 2022; Liu et al., 2020; Sun et al., 2023), China has intensified the construction of large-scale underground oil and natural gas storage facilities, particularly salt cavern-type energy

storage, to enhance the ability to address energy security risks and ensure sustainable development of the national economy and society.

Salt caverns are widely used for underground energy storage worldwide (Firme et al., 2019; Ozarslan, 2012; Wang et al., 2019), including oil, hydrogen, natural gas and compressed air energy storage. This is due to their self-healing ability to repair host rock damage (Chen et al., 2020b; Han et al., 2021), good sealing performance (Li et al., 2020), high plasticity, and stable chemical and physical properties (Zhang et al., 2014). Salt caverns can also be utilized for industrial solid waste and nuclear waste disposal (Shahmorad et al., 2016; Shi et al., 2015) as well as CO<sub>2</sub> sequestration (da Costa et al., 2011). In China, salt rock reservoirs are typically constructed by the single-well convection water-soluble mining method with a diesel cushion to protect the cavern roof (Brouard

\* Corresponding author. College of Energy and Mining Engineering, Shandong University of Science and Technology, Qingdao, 266590, Shandong, China.

E-mail address: [gexinbo@sdust.edu.cn](mailto:gexinbo@sdust.edu.cn) (X.-B. Ge).

et al., 1997; Wang et al., 2018a, 2018b). As illustrated in Fig. 1, fresh water is injected into the cavern through the inner tubing (or annulus between the inner tubing and the outer tubing), while brine flows from the annulus (or the inner tubing) to the ground, known as direct circulation (or reverse circulation) (Li et al., 2019). The volume of caverns gradually expands as salt rock on the cavern wall continuously dissolves in the flowing unsaturated brine. The direct and reverse circulation methods are used alternately until the construction of the salt cavern is completed.

The leaching tubing may encounter engineering accidents such as excessive bending or damage during direct circulation or reverse circulation. For example, between 1980 and 2000, there were 22 instances of leaching tubing failures due to flow-induced vibration during the construction of salt caverns in the Sorrento salt dome (Evans and Chadwick, 2009). Similarly, from 2009 to 2017, during the construction of Jiangnan Salt Cavern Gas Storages, there were four gas storage wells that underwent 25 tubing-inspection operations. Out of these, 22 tubing-inspection operations revealed excessive deformation of the leaching tubing, leading to excessive load or breakage during tubing removal. Fig. 2 illustrates engineering accidents of leaching tubings in Chinese salt cavern storages, such as excessive bending, fracture, and coupling damage. During workover operations, if the inner tubing is excessively bent, it may be difficult to lift it in a limited space, causing damage to the outer tubing. Therefore, in engineering, severely bent inner tubings sometimes have to be cut and permanently discarded in the salt cavern. Excessive bending or damage of the leaching tubing not only increases the cost and duration of leaching, but also raises the likelihood of irregularly shaped salt caverns.

Excessive bending or damage of the leaching tubing is primarily

caused by the flow-induced vibration instability (Ge et al., 2019). Previous research by Li et al. (2016a, 2016b) has focused on laboratory simulation experiments of the liquid-solid coupling of leaching tubings. However, due to equipment limitations, they were unable to observe the flutter instability of the cantilevered pipe conveying fluid. To address this, Ge et al. (2019) developed an indoor simulation apparatus for leaching tubing and conducted a series of experiments using silicone-rubber pipes (SRPs) and polycarbonate pipes (PCPs) with different lengths and diameters. They verified the reliability of the experimental apparatus under unconstrained conditions in air. In a subsequent study, Ge et al. (2021) established the dynamic equation of leaching tubing with a Y-type manifold installed at the lower free end. The physical model experiment, conducted using the laboratory apparatus developed by Ge et al. (2019), confirmed that the Y-type manifold greatly enhances the stability of the leaching tubing. Furthermore, the experimental flutter critical flow velocity closely corresponded to the theoretical value. Fig. 1 illustrates that the inner tubing are immersed in brine, experiencing the simultaneous effects of axial internal flow and outer flow, while being partially restricted by the space of the outer tubing. Considering the unique structural characteristics of the leaching tubing, several research papers on fluid-conveying pipes similar to the leaching tubing were reviewed.

The study of vertical cantilevered pipes carrying axial fluid flow has been extensively conducted in recent decades (Moditis et al., 2016; Païdoussis, 2014). Various cases have been examined in these studies, which are of significant reference value for investigating the characteristics of flow-induced vibration and stability control of the leaching tubing. These cases include pipes that are partially or fully submerged in water, pipes equipped with an

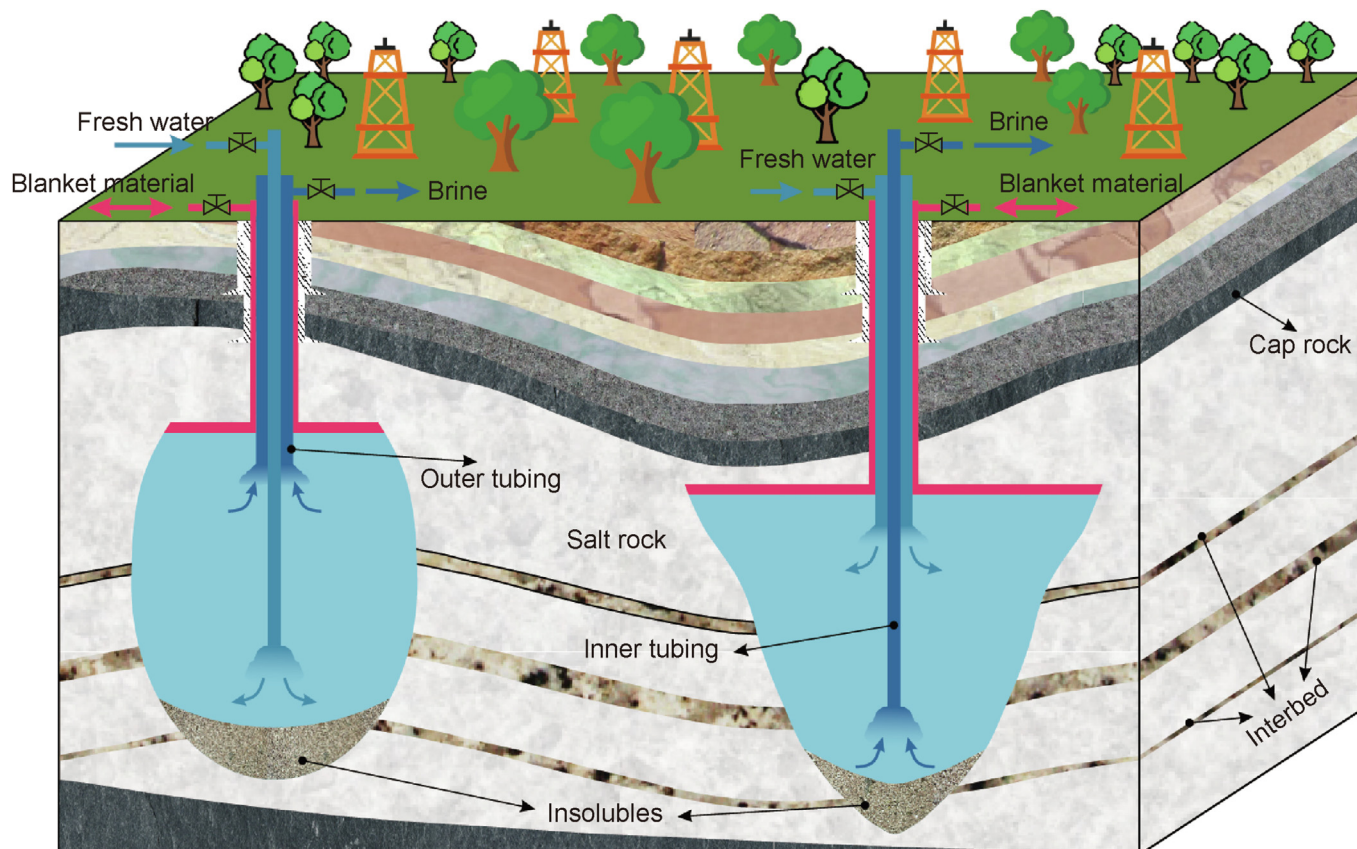


Fig. 1. Schematic illustration of leaching tubing systems for the construction of a single-well salt cavern by water leaching.



**Fig. 2.** Failure accidents of leaching tubings in the site of salt cavern gas storages, (a) excessive bending, (b) fractured outer tubing, (c) coupling damage (Ge et al., 2021).

inclined nozzle at the free end, pipes with a normal end-nozzle, pipes with multiple masses attached along the length, a Y-shaped tube, pipes with a mass attached at the free end, and pipes with a variable supports.

Lundgren et al. (1979) conducted a theoretical and experimental study on self-induced non-planar vibrations of a flexible fluid-conveying tube. The tube is vertically cantilevered with a nozzle at the free end inclined to the axis of the tube. Hannyer and Païdoussis (1979b) proposed a comprehensive theory to analyze the dynamics of slender, nonuniform axisymmetric beams under the influence of internal or external flow, or both simultaneously. In parallel, Hannyer and Païdoussis (1979a) conducted experimental research to validate the theoretical findings presented by (Hannyer and Païdoussis, 1979b). The experimental results qualitatively align closely with the theoretical predictions. Edelstein and Chen (1985) developed equations that govern the dynamics of a horizontally cantilevered tube conveying fluid, with a variable knife-edge support movable along the tube. Jendrzeczyk and Chen (1985) performed tests to investigate the stability of vertically cantilevered tubes with a knife-edge support movable along the tube. Sugiyama et al. (1996) investigated the flutter behavior of vertical beam-type pipes conveying a flowing fluid, with their lower end immersed in fluid. Water-conveying experiments were conducted using silicone-rubber tubes to investigate the effects of the immersed length on the critical flutter velocity and to verify the theoretical predictions. Yoshizawa et al. (1998) conducted a study on the vibration of a vertical cantilevered pipe conveying fluid with an end mass using both theoretical and experimental methods. They discussed the influence of the end mass by analyzing the

nonlinear coupling equations that control the vibration of non-planar pipes. The researchers conducted experiments with a water-conveying SRP and observed the spatial behaviors of the SRP using an image-processing system. In a separate study, Xu and Huang (2000) focused on the theoretical analysis of planar vibration motions of a straight vertical cantilevered pipe that conveys a steady fluid. The pipe was clamped at one end and had a nozzle subjected to nonlinear constraints at the free end. Modarres-Sadeghi et al. (2007) explored the three-dimensional dynamics of a cantilevered fluid-conveying pipe with an additional 'point' mass at the free end using theoretical methods. Kuiper and Metrikine (2008) designed a new test set-up to investigate the dynamic stability of a cantilevered fluid-aspirating pipe. They used a plastic pipe of approximately 5 m length, with the fixed end above the waterline and the free open end submerged in the water. When the water convection through the pipe exceeded the critical velocity, they observed a nearly periodic orbital motion and a noise-like vibration.

In recent years, there has been a continued interest in studying the dynamic characteristics of vertical cantilever pipes conveying fluid. Rinaldi and Païdoussis (2010) conducted both theoretical and experimental investigations on the flow-induced vibration of a flexible cantilevered pipe. The pipe had a special end-piece at the downstream end, which could be used either in its 'unplugged' configuration, where fluid was discharged straight at the free end as a jet, or in the 'plugged' mode, allowing flow to exit via side-holes perpendicular to the pipe axis. Ibrahim (2010, 2011) provided a comprehensive overview of fluid-conveying pipes, covering various types of modeling, dynamic analysis, and stability regimes.

The article also explored the fluidelastic instability in both single- and two-phase flows, as well as fretting wear in process equipment. Wang and Dai (2012) conducted a theoretical investigation on the properties of flow-induced vibration of horizontal pipes conveying fluid and having two symmetric elbows at downstream end. Their findings revealed that the stability of the pipes was significantly improved with the presence of these symmetric elbows. In another theoretical study, Firouz-Abadi et al. (2013) examined the coupled bending-torsional vibrations of a horizontal cantilevered fluid-conveying pipe equipped with an inclined terminal nozzle at the downstream end. They determined the impact of various factors such as nozzle aspect ratio, bending-to-torsional rigidity ratio, nozzle inclination angle and mass ratio on the flutter velocity of the pipe system. Wang et al. (2014) developed a static analysis model to analyze the stress and deformation in the installation of a riser. They considered the riser as a beam subjected to both axial and lateral forces, suspended in a floating drilling platform (ship). Mao et al. (2016) treated a drilling riser with the actual riser string configuration as a simply supported beam subjected to lateral and axial ocean environment loadings, and located in the vertical plane. They conducted a test in a deep-water basin using polyvinyl chloride to obtain the mechanical behavior of the drilling riser. Fan et al. (2017) constructed a dynamic model of a hang-off drilling riser based on the Euler-Bernoulli theory, taking into account vessel motion and the combined excitation of internal solitary waves, surface waves, and ocean currents. Askarian et al. (2020) carried out a theoretical investigation on the bending-torsional stability of a cantilevered pipe conveying fluid with an inclined end-nozzle, as well as simultaneous internal axial and external cross flows. Khudayarov et al. (2020) developed a mathematical model and a numerical algorithm to analyze the vibration of a composite pipeline conveying a pulsating fluid flow on a viscoelastic base. Païdoussis et al. (2021) conducted a study on the dynamics of a vertical cantilevered pipe conveying fluid. The pipe was subject to both axial inflow and axial outflow and was located in a container filled with the same fluid. The study focused on the stability of the system, and it was conducted using both theoretical and experimental methods. Païdoussis (2022) provided a concise overview of the basic principles governing the dynamics of fluid-conveying pipes. Additionally, the author delves into a comprehensive examination of the latest research in this field, highlighting the diverse range of systems under investigation. Shaaban et al. (2023) conducted an experimental study to explore the impact of imperfections in the clamping of cantilevered pipes that discharge or aspirate fluid. The investigation encompassed six distinct scenarios. Research efforts (Païdoussis, 2022; Païdoussis et al., 2021; Shaaban et al., 2023) have significantly contributed to our understanding of the dynamic characteristics of the leaching tubing. However, there are still several unresolved issues, particularly the investigation of hydrodynamic damping experienced by the suspended leaching tubing in the liquid.

This article presents a series of experiments using SRPs and PCPs under different configurations (shown in Fig. 6), based on the experimental laboratory apparatus developed by Ge et al. (2019) for investigating the dynamics of the leaching tubing. This paper is a companion paper of previously published papers by Ge et al. (2019, 2021). The experiments include scenarios such as pipes totally immersed in water, pipes with an external space constraint and pipes with a Y-shaped or T-shaped end. The dynamic characteristics of these fluid-conveying pipes are discussed, and the critical flow velocity is analyzed. The research results in this paper are expected to provide valuable insights for the prevention and control of flow-induced vibration instability of the leaching tubing.

## 2. Model for the inner tubing under ideal conditions

The gap between the inner tubing and outer tubing is relatively small, ranging from 24 to 60 mm, as shown in Fig. 1. The inner tubing is confined within the outer tubing from the ground to the top of the salt cavern. Within a salt cavern, the inner tubing is partially confined within the outer tubing, and the lower end of the outer tubing is positioned at a certain distance from the top of the salt cavern. During the later stages of leaching, the lower end of the outer tubing will be slightly lower than the diesel cushion. At this point, the inner tubing functions as a regular pipe for conveying axial internal flow without any restrictions. Assuming the leaching tubing is fixed at the casing shoe, the inner tubing can be simplified to a fluid-conveying pipe model illustrated in Fig. 3. In this simplified model, we consider the influence of gravity while neglecting internal dissipation in the pipe material, damping associated with the presence of an external fluid, the external confined space, and axial outer flow. The governing equation for the simplified inner tubing is (Païdoussis, 1970):

$$EI \frac{\partial^4 Y}{\partial X^4} + [MU^2 - g(M + m)(L - X)] \frac{\partial^2 Y}{\partial X^2} + g(M + m) \frac{\partial Y}{\partial X} + 2MU \frac{\partial^2 Y}{\partial X \partial t} + (M + m) \frac{\partial^2 Y}{\partial t^2} = 0 \quad (1)$$

Here  $EI$  is the flexural rigidity,  $m$  is the mass of the pipe per unit length,  $M$  is the mass of water in the pipe per unit length,  $U$  is flow velocity in the pipe,  $L$  is the length of pipe,  $X$  is longitudinal coordinate,  $Y$  is lateral deflection of the pipe,  $g$  is gravity, and  $t$  is time.

A set of dimensionless terms are used to transform Eq. (1) to a non-dimensional form, and the detailed solution process of Eq. (1) can be found in (Doaré and De Langre, 2002; Païdoussis, 1970). As shown in Fig. 4 (Païdoussis, 1970), the dynamics of the fluid-conveying pipe system (Fig. 3) depends on three parameters:  $\beta$ , the non-dimensional mass ratio, where  $0 < \beta < 1$ ;  $\gamma$ , which depends on the gravimetric and flexural properties of the system; and  $u$ , the dimensionless flow velocity.  $\beta$ ,  $\gamma$  and  $u$  are respectively expressed as

$$\beta = \frac{M}{M + m}, \gamma = \frac{(M + m)g}{EI} L^3, u = UL \left( \frac{M}{EI} \right)^{\frac{1}{2}} \quad (2)$$

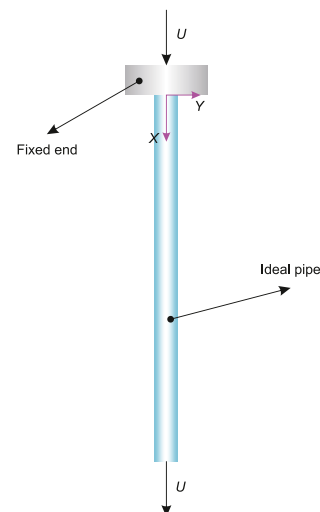


Fig. 3. Ideal model for the inner tubing.

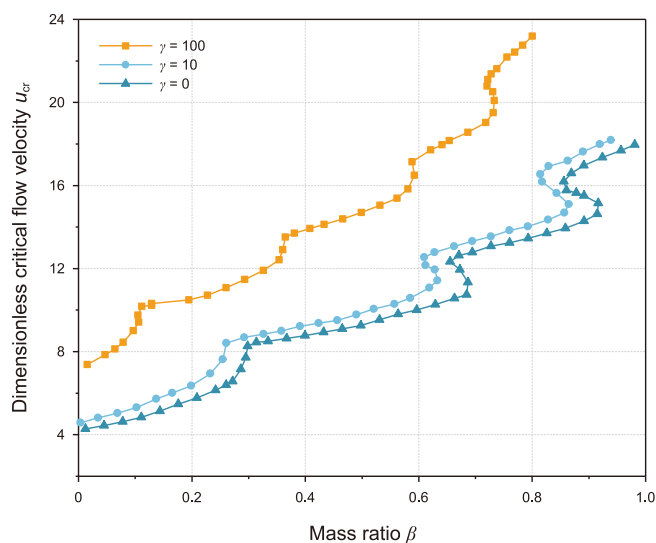


Fig. 4. Variation of the non-dimensional critical flow velocity for flutter instability with mass ratio  $\beta$  under different  $\gamma$  (Paidoussis, 1970).

### 3. Experimental facility

An experimental apparatus (Fig. 5) was developed to investigate the flow-induced vibration dynamics of the leaching tubing. The apparatus was described in detail in a paper published by Ge et al. (2019). The effectiveness and reliability of the device were verified by two sets of preliminary experiments conducted by Ge et al. (2019). A series of experiments presented in this article were carried out using this apparatus.

### 4. Experimental procedures and results

A series of experiments were conducted using flexible pipes, that is, specifically SRPs and PCPs. SRPs and PCPs are custom-made at the manufacturing plant using the extrusion molding process. They are not wound on rollers but instead placed in a long wooden

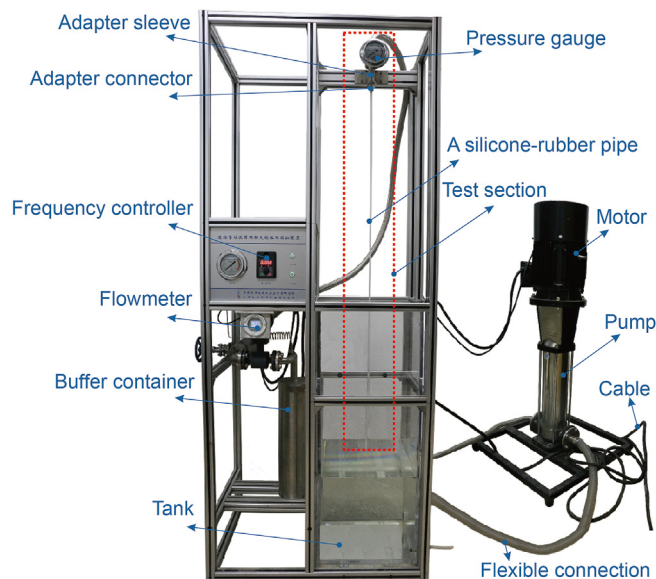


Fig. 5. Photograph of an experimental laboratory device for the leaching tubing (Ge et al., 2019).

box. When suspended, both the SRP and PCP appear to be essentially straight, although there may be a small amount of locked-in stress present in them. No special stress-relieving measures were taken for the SRP and PCP. Therefore, in this paper, plastic materials (i.e. silicone rubber and polycarbonate) pipe and real leaching tubing is the geometric similarity. The fluid conveyed in the pipes was tap water with a density of approximately  $1000 \text{ kg/m}^3$ . Table 1 provides a summary of the properties of SRPs and PCPs. Various experiments were performed using pipes with different inner diameters and lengths, under different configurations (as shown in Fig. 6), in order to determine the influence of certain parameters on the stability of the pipes. These parameters include the medium outside the pipe, external space constraint, end-piece shape, and combinations of these factors. The experiments conducted in this paper can be broadly classified into three configurations. A detailed description and graphic illustration of all the different configurations are provided in Table 2 and Fig. 6, respectively. The experiments were carried out following a series of steps, including installing the test pipe, adjusting the pump frequency, reading pressure and flow rate, collecting vibration amplitude of the pipe, observing and recording experimental phenomena, and capturing relevant photos/videos.

#### 4.1. Experiments without confinement in air

In the case of Config. 1a, pipes with different lengths, labeled as 1#, 2#, and 3#, were used in the experiments. As the flow velocity in the pipe gradually increased from zero, various fluid-solid coupling phenomena were observed at certain flow velocities. These included water hammer, static buckling, flutter instability, and chaotic motion. For a detailed analysis, please refer to Ge et al. (2019). The experiment conducted Config.1a serves as the control experiment in this article.

Fig. 7 illustrates the theoretical and experimental values of the critical flutter velocity for pipes with a certain mass ratio  $\beta$ , as the dimensional length ( $L$ ) changes. The theoretical value is obtained using Eq. (1), based on the prediction of the first instability. In Fig. 7(a), it can be observed that the change trend of the theoretical value of the critical flutter velocity for the SRP is consistent with the experimental value, indicating a good agreement. When the dimension length ( $L$ ) is sufficiently long, the theoretical value of the critical flutter velocity tends to approach a progressive value similar to the experimental value. The phenomenon of the curve in Fig. 7(a) approaching asymptotic values has been previously discussed and explained by Doaré and De Langre (2002). In their investigation, Doaré and De Langre (2002) examined the impact of increasing length on the stability of a hanging pipe conveying fluid. Similarly, in Fig. 7(b), the theoretical value of the critical flutter velocity for the PCP is generally consistent with the experimental value, showing a consistent change trend. However, due to limitations in the experimental apparatus, the maximum length of the pipe used is only 2 m. Therefore, in Fig. 7(b), it is not possible to observe the tendency of the critical flutter velocity to approach a progressive value with the change in length ( $L$ ) for the PCP.

#### 4.2. Experiments with different end-piece shape in air

During cavern leaching, there are instances where the engineering requirements necessitate transforming the end of the inner leaching tubing into a penpoint-like shape. This modification facilitates the insertion of the tubing into the sediment at the bottom of the salt cavern, as depicted in Fig. 8(a). In cases where reverse circulation water injection is employed for cavern leaching, a filter screen is installed at the end of the inner leaching tubing. This screen serves the purpose of preventing large rock blocks from

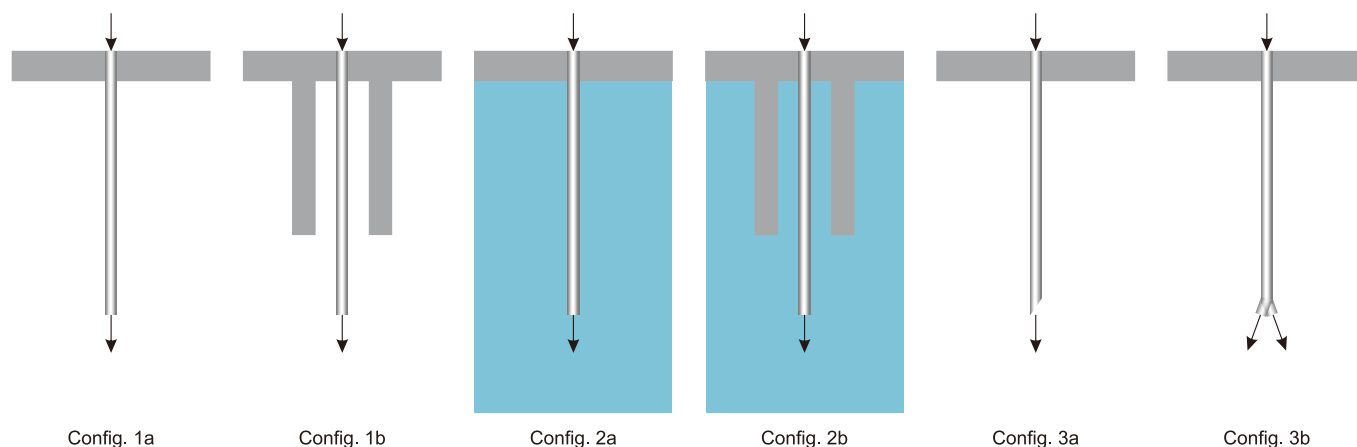


Fig. 6. Graphic illustration of different experimental configurations.

Table 1  
The geometrical and physical properties of pipes.

| Material | No. | $EI, N \cdot m^2$ | $D, mm$ | $d, mm$ | $m, kg/m$ | $M, kg/m$ | $\beta$ |
|----------|-----|-------------------|---------|---------|-----------|-----------|---------|
| SRP      | 1#  | 8.60E-04          | 9.01    | 5.02    | 5.61E-02  | 1.96E-02  | 0.26    |
|          | 2#  | 5.29E-03          | 14.02   | 9.98    | 1.02E-01  | 7.85E-02  | 0.44    |
| PCP      | 3#  | 5.45E-02          | 5.01    | 3.42    | 1.23E-02  | 9.08E-03  | 0.42    |

entering the tubing and causing blockages, as shown in Fig. 8(b). The objective of this paper is to experimentally investigate the dynamic response behavior of fluid-structure coupling in cantilevered fluid-conveying pipes with two different end shapes. These shapes include a penpoint-like end and two bifurcated ends: an

Table 2  
Different experimental configurations.

| Configuration | Description   |
|---------------|---|
| 1             | Reference case for other configurations. A cantilevered pipe discharging water is surrounded by air in two ways, namely, (a) without external space constraint; (b) with an external rigid pipe extending from 0 to $L$ . |
| 2             | Similar to Config. 1, but the pipe is surrounded by water in two ways, namely, (a) without confinement; (b) with an external rigid pipe extending from 0 to $L$ .   |
| 3             | Similar to Config. 1, but the free end is different, namely, (a) having a penpoint-like end, (b) having a bifurcated end, namely Y-shaped end or T-shaped end.  |

inverted Y-typed end and an inverted T-typed end.

4.2.1. Penpoint-like end

In the experiments conducted under the conditions of Config. 3a, the 2# SRPs and 3# PCPs were utilized. The lengths of the SRPs were 1.61, 1.01, and 0.61 m, while the lengths of the PCPs were 1.61, 1.41, and 1.21 m, respectively. The pipe end was transformed into the shape illustrated in Fig. 9.

The experiment was conducted following the specified operating steps. By gradually adjusting the pump frequency, the flow velocity in the pipe increased from zero, leading to flutter instability in both SRPs and the PCPs. Additionally, both SRPs and PCPs underwent a similar buckling process as described by Ge et al.

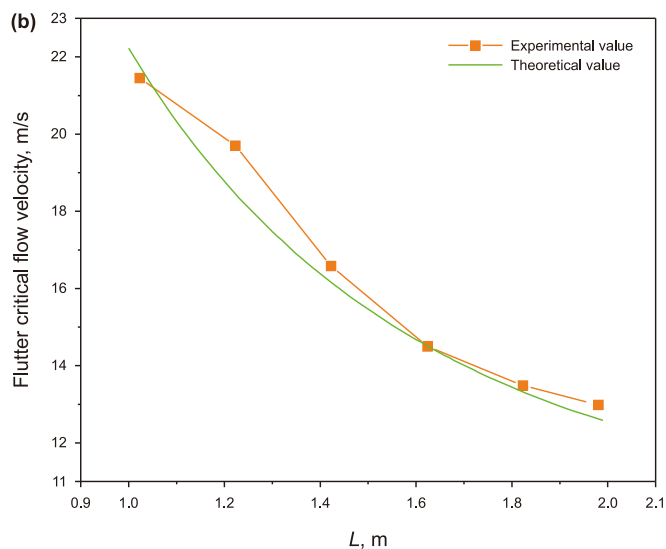
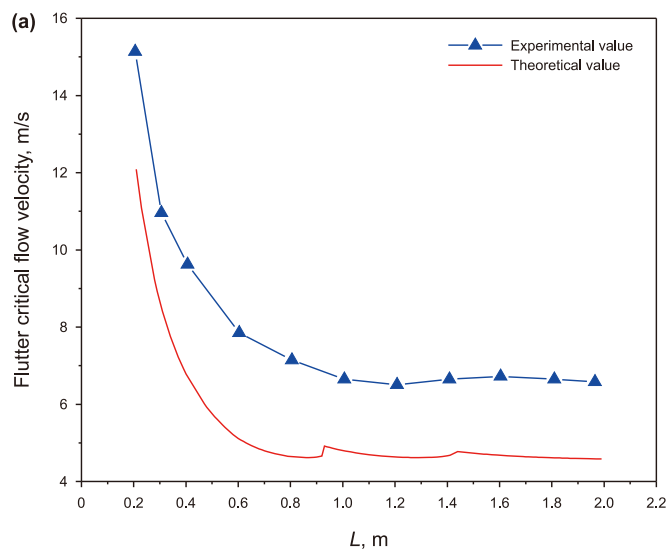


Fig. 7. Experimental values and theoretical values of flutter critical flow velocity, (a) SRPs with  $D = 5.02 mm$ , (b) PCPs with  $d = 3.42 mm$ .



Fig. 8. Two end forms of the inner tubing in engineering site.

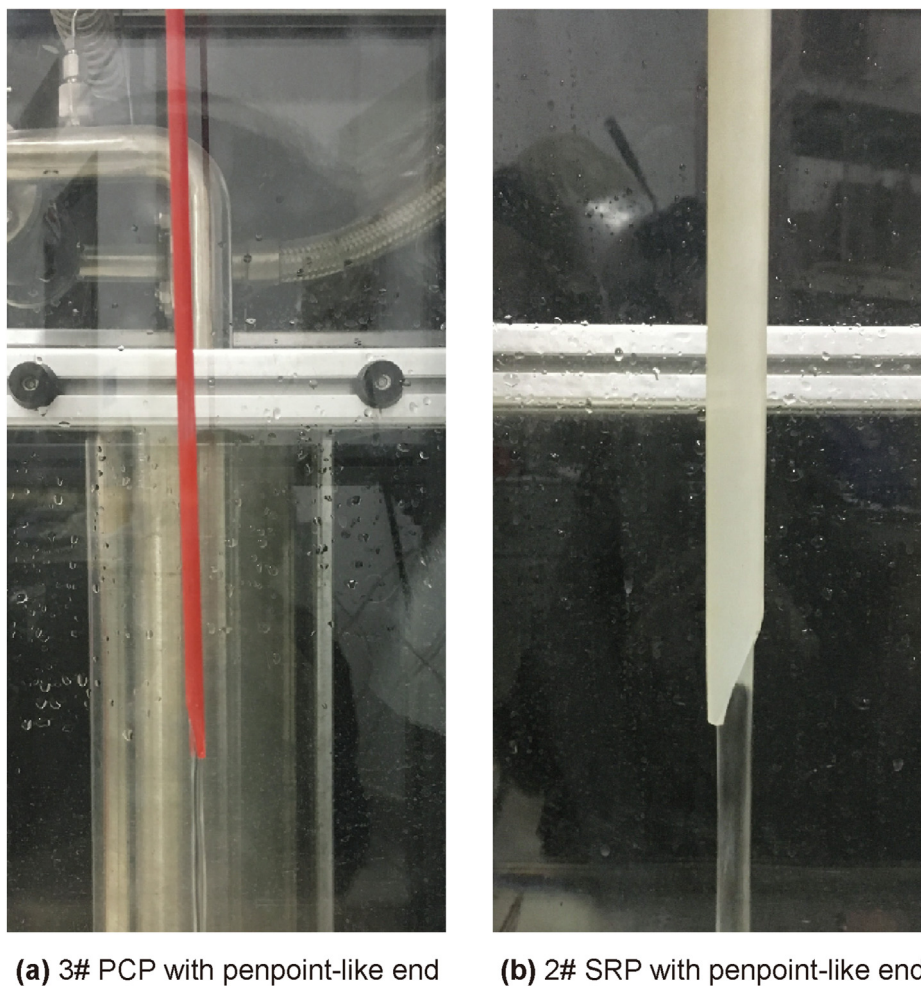


Fig. 9. Penpoint-like end form of PCPs and SRPs.

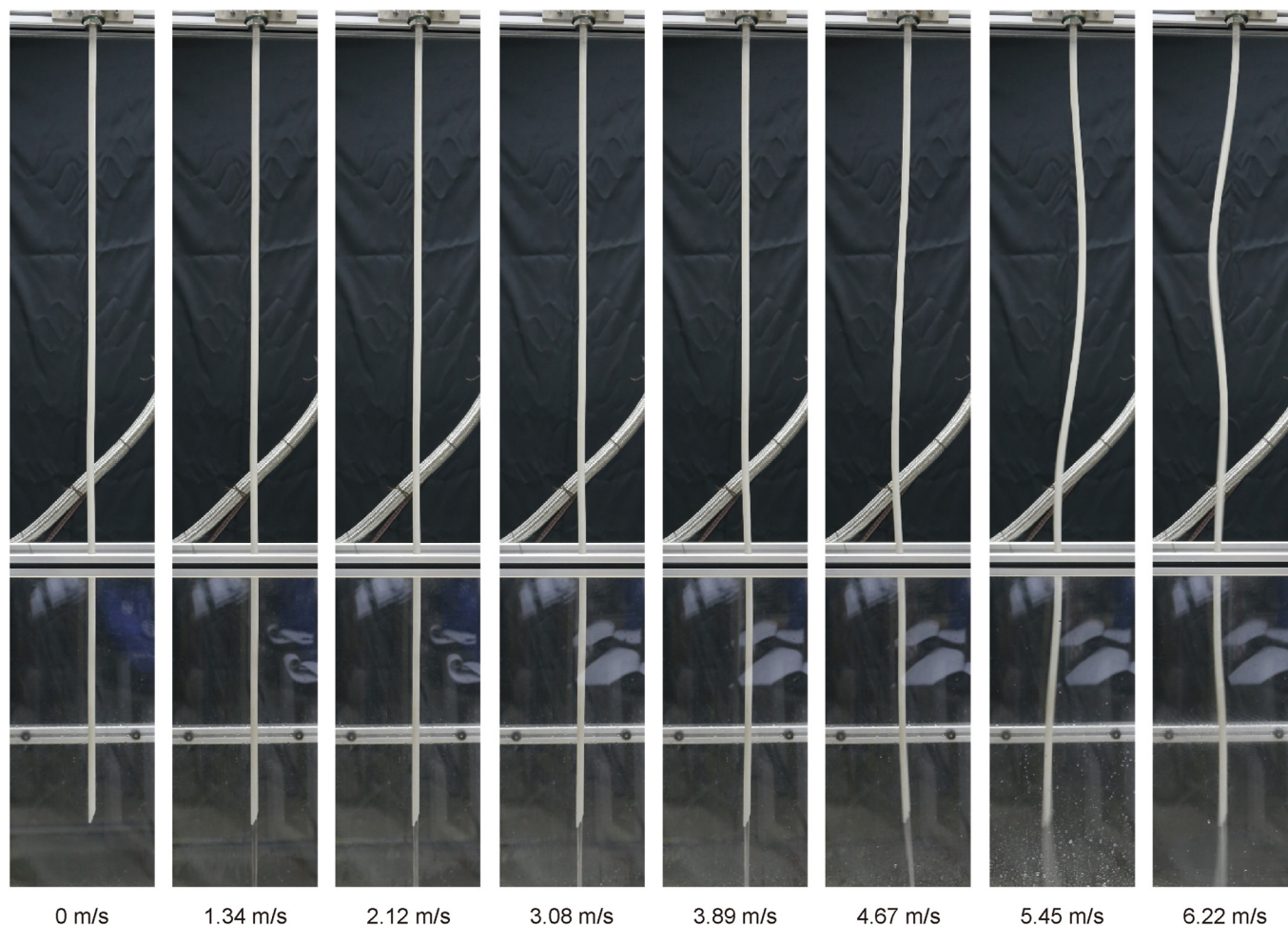


Fig. 10. Bending of a 1.61 m 2<sup>#</sup> SRP with a penpoint-like end before flutter occurring in the air.

(2019) prior to the occurrence of flutter instability. Fig. 10 illustrates the buckling process of a 1.61 m 2<sup>#</sup> SRP with a penpoint-like end. This section primarily focuses on whether the critical flutter velocity of SRPs and PCPs is affected by the shape of the penpoint-like end. However, it does not address the water hammer phenomenon, buckling process, or chaotic movement.

All the test pipes with penpoint-like end exhibited flutter instability. The flutter critical flow velocity of pipes with normal end and penpoint-like end is compared in Fig. 11. It can be observed that the flutter critical flow velocity in both cases is essentially the same. Considering the potential error of the experiment system itself and the influence of other unknown factors, the difference between the flutter critical flow velocities in the two cases is acceptable. Therefore, the penpoint-like end has little effect on the flutter critical flow velocity of cantilevered pipes conveying fluid.

#### 4.2.2. Bifurcated end

In the experiments conducted in Config. 3b, the 2<sup>#</sup> SRPs with a length of 1.61 m and fitted with bifurcated ends were used. The flutter critical flow velocity of a 2<sup>#</sup> SRP with a length of 1.61 m under the case of Config. 1a is 6.12 m/s. The bifurcated end used here has an inner diameter of 9.63 mm, as shown in Fig. 12. Bifurcated ends can be classified into inverted Y-typed ends (such as Fig. 12(a), (c)) and inverted T-typed ends (such as Fig. 12(b), (d)). When the bifurcated end has the same inner diameter, different bifurcated arm lengths are set, as illustrated by the difference

between Fig. 12(a) and (c). For more detailed theoretical and experimental analyses, refer to the paper by Ge et al. (2021).

4.2.2.1. (1) *Inverted Y-typed ends.* Significant buckling occurred in the experiment when using a 2<sup>#</sup> SRP with an inverted Y-type end with a long arm. The buckling phenomenon became more apparent as the flow velocity in the pipe gradually increased from zero by adjusting the pump frequency, as shown in Fig. 13. However, it was observed that the downstream end of the SRP touched the wall of the tank only when the flow velocity in the pipe reached 10.15 m/s, which was significantly greater than 6.12 m/s. At this point, the SRP began to beat against the wall of the tank without any flutter beforehand. This indicates that the flutter critical flow velocity has increased due to the presence of the inverted Y-type end with a long arm, but it also makes the fluid-conveying pipe more susceptible to noticeable and severe buckling.

When using the inverted Y-type end with a short arm, the 2<sup>#</sup> SRP conveying fluid also experienced buckling as the flow velocity in the pipe gradually increased from zero, as shown in Fig. 14. It was observed that the SRP experienced flutter instability when the flow velocity in the pipe reached 6.30 m/s, slightly greater than 6.12 m/s. This suggests that the presence of the inverted Y-type end with a short arm can also increase the flutter critical flow velocity, although the effect is not as pronounced as that with a long arm. Furthermore, both inverted Y-types ends with short or long arms make SRPs more prone to noticeable and severe buckling.

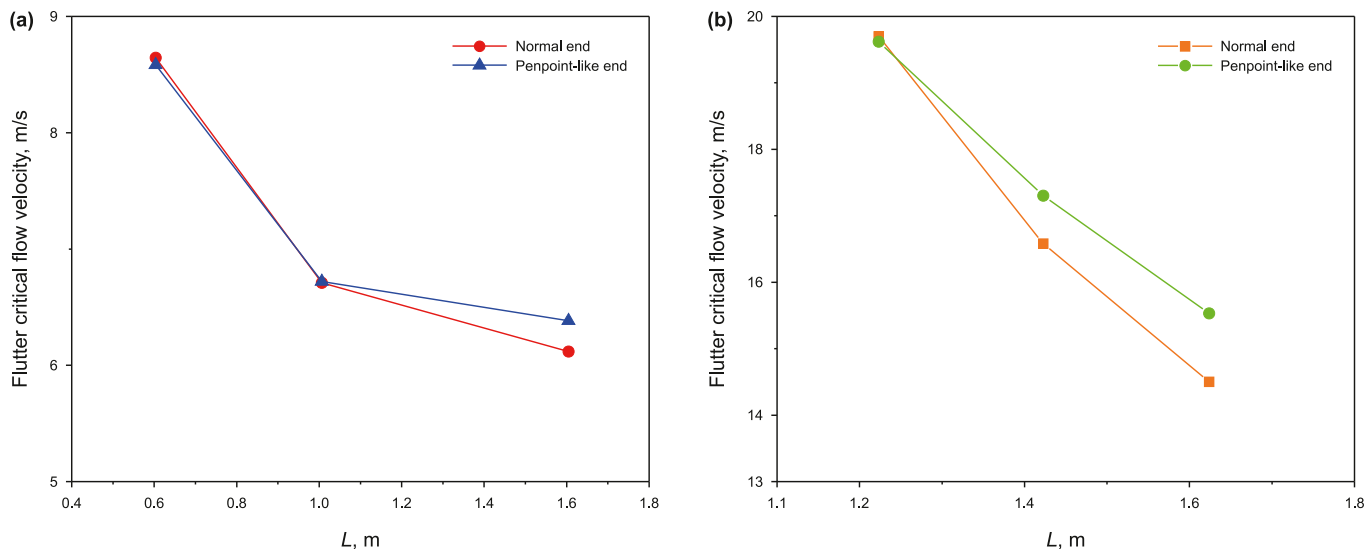


Fig. 11. Comparison of flutter critical flow velocity between Penpoint-like end and normal end, (a) SRPs, (b) PCPs.

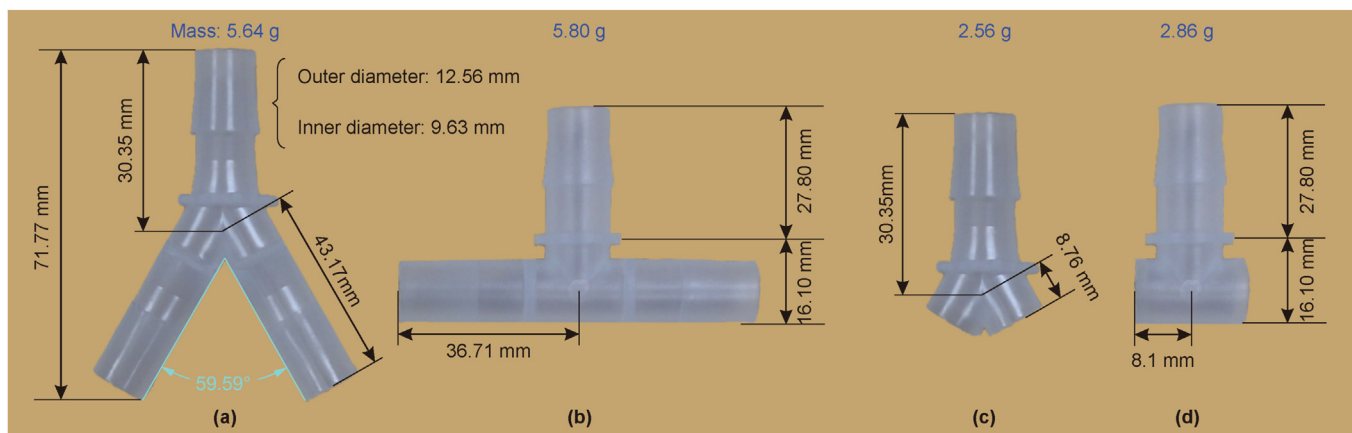


Fig. 12. Bifurcated ends with internal diameter 9.63 mm (Ge et al., 2021).

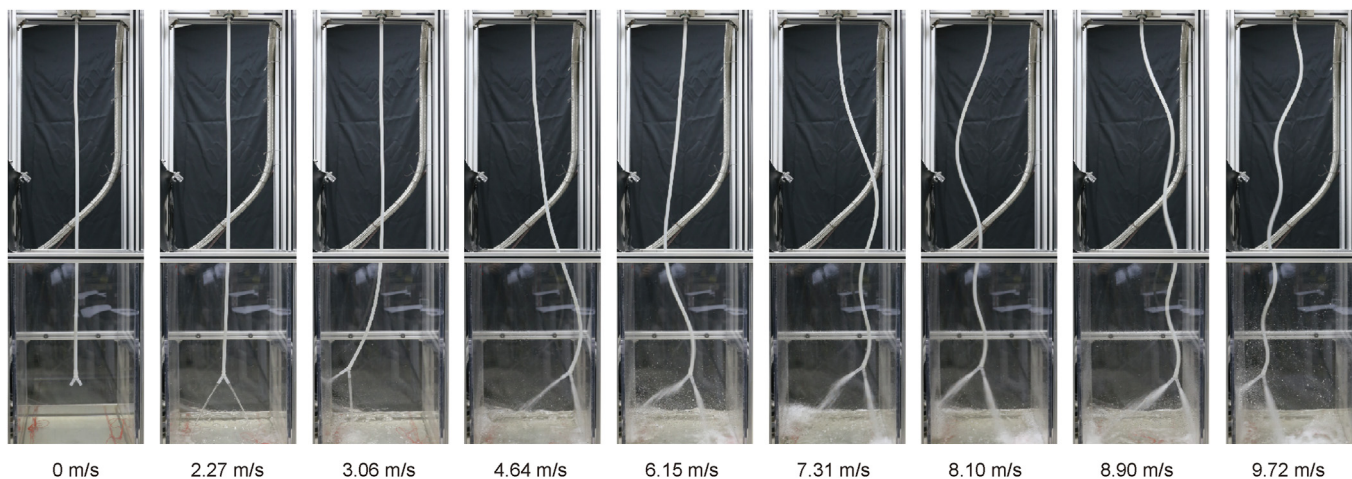


Fig. 13. Bending change under an inverted Y-type end with long arm (Ge et al., 2021).

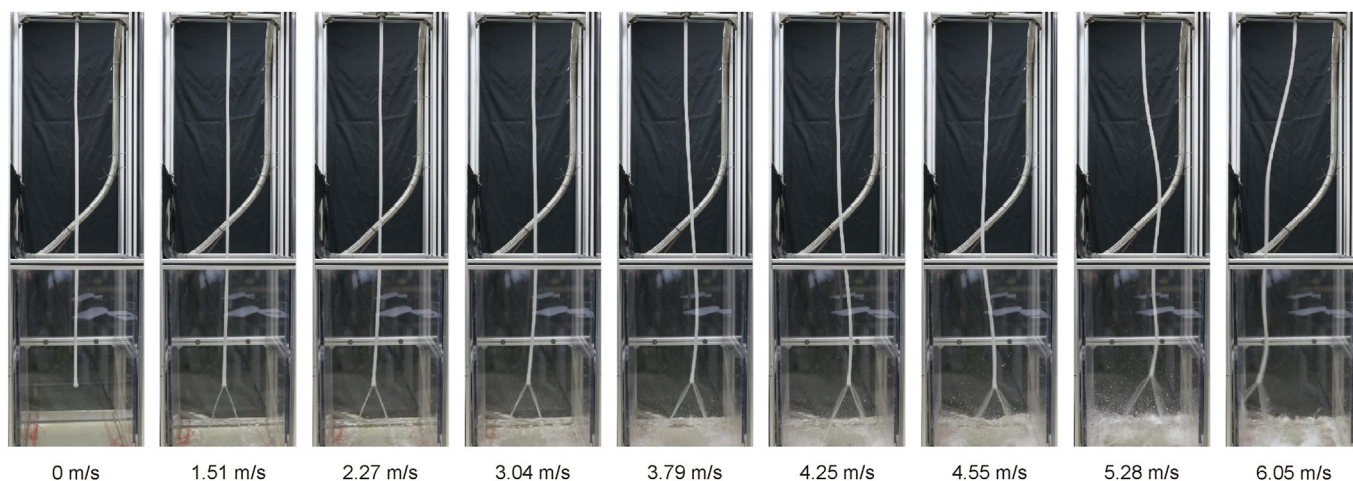


Fig. 14. Bending change under an inverted Y-type end with short arm (Ge et al., 2021).

4.2.2.2. (2) *Inverted T-typed ends.* When utilizing the inverted T-type end, the SRP did not experience any flutter instability, even when the flow velocity in the pipe was significantly higher than the critical flow velocity for flutter with a normal end. Additionally, as the flow velocity in the pipe gradually increased from zero, there was no noticeable buckling process. However, the downstream end shifted to the left, as depicted in Fig. 15. When the vertical water flow passed through the inverted T-type end, it turned vertically and flowed along both side-channels of the T-type end. The impact of the water flow at the bottom of the inverted T-type end caused the SRP straighten to remain straight, preventing buckling. Furthermore, as the flow velocity in the SRP increased, the water flow velocity on the right side-channel of the inverted T-type end exceeded that on the left side, resulting in the leftward shift of the downstream end of the SRP. In the case of the inverted T-type end with a long arm, when it shifted too far to the left and touched the wall of the tank, the flow velocity in the SRP was 8.75 m/s (clearly greater than 6.12 m/s), yet no flutter instability was observed. Increasing the flow velocity in the SRP further caused the left side of the inverted T-type end to consistently remain attached to the tank wall, and still no flutter instability occurred, leading to the termination of the experiment. These results confirm the radial discharge findings by Rinaldi and Païdoussis (2010) in the ‘plugged’ mode, where flow exits through side-holes perpendicular to the pipe axis.

A similar phenomenon to Fig. 15 was also observed when using the inverted T-type end with a short arm (Fig. 12(d)).

#### 4.3. Experiments with confinement in air

In the experiments in Config. 1b, a transparent acrylic pipe was used as an external space constraint, as depicted in Fig. 16. The test pipes, namely the 2<sup>#</sup> SRP and 3<sup>#</sup> PCP, were utilized, with the test pipe being partially confined within the transparent acrylic pipe. The parameter combination of the test pipes and the external space constraint is summarized in Table 3.

The flow velocity in test pipes with external space constraint gradually increases as the pump frequency is slowly increased. The experiment is terminated either when the test pipes experience flutter instability or when the equipment is close to the limit state. Regardless of the length of the external space constraint, the SRPs buckle during the process of gradually increasing the flow velocity. Initially, the SRP does not come into contact with the transparent acrylic pipe, but after buckling, it makes contact. Fig. 17 illustrates the buckling state of the SRP at a high flow velocity before fluttering under different lengths of external space constraint. When the external space constraint is shorter, (e.g. 0.2 m), the buckling state of the unconstrained part of the SRP is similar to that without external space constraint (details in (Ge et al., 2019)). Conversely,

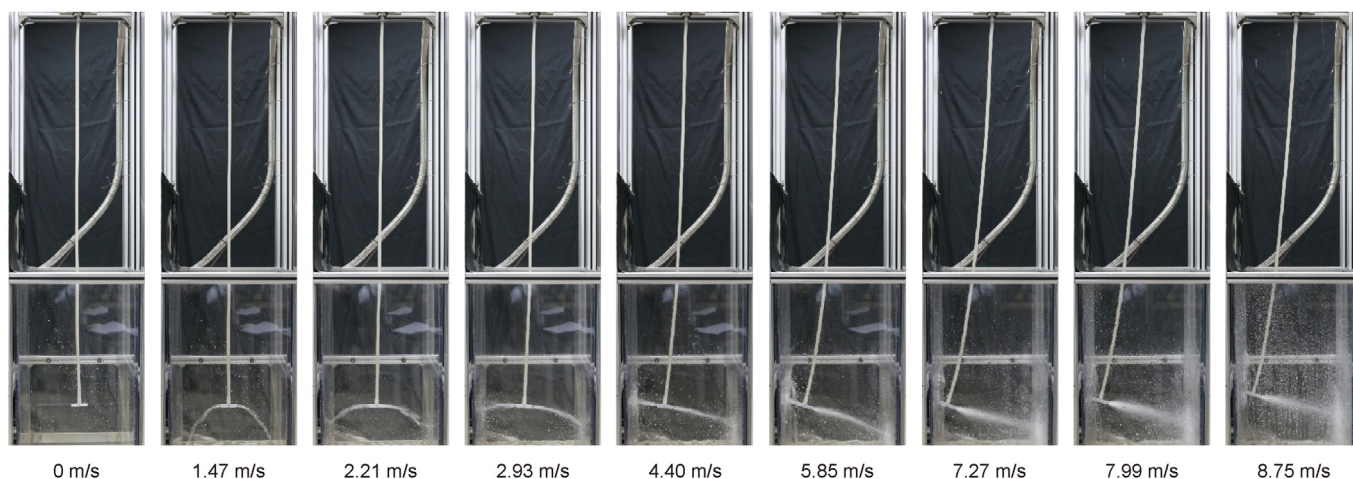
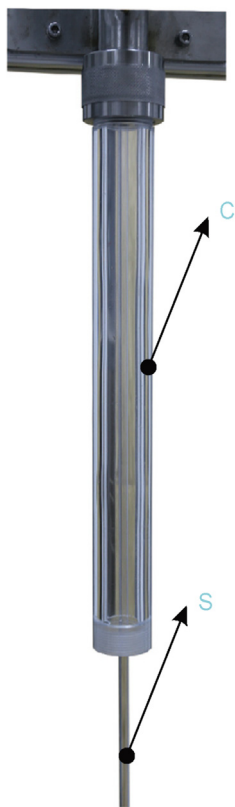


Fig. 15. Free end sideways under an inverted T-type end with long arm (Ge et al., 2021).



**Fig. 16.** The test pipe installed with an external space constraint. C: confinement of transparent acrylic pipe. S: SRP or PCP (Ge et al., 2019).

when the external space constraint is longer, (e.g. a ratio of the external space constraint length to the SRP length is greater), the buckling of the SRP is restricted by the annular space, and the unconstrained part of the SRP is less likely to buckle, remaining in a straight state as observed when the external space constraint length is 1.4 m. In the case of the external space constraint length of 1.4 m, when the pump frequency reaches 43 (with a maximum pump frequency of 50), the SRP falls off the connecting end without experiencing flutter. Since the 2<sup>#</sup> SRP with a length of 0.2 m did not suffer from flutter instability when there was no external space constraint, this set of experiments was not repeated. A similar phenomenon was observed in a paper by Pettigrew and Paidoussis (1975). The study demonstrated that a flexible cylinder, when subjected to axial flow in confined annuli, would buckle against the wall of the test section at multiple points depending on the mode order. Subsequently, the free end of the cylinder would vibrate from the last point of contact.

In all cases with external space constraints, the PCPs buckled as the flow velocity gradually increased. With the exception of the 0.2 m external space constraint, the PCP initially did not come into contact with the transparent acrylic pipe, but after buckling, it touched the transparent acrylic pipe. Fig. 18 illustrates the buckling state of the PCP at a high flow velocity before fluttering under

different lengths of external space constraint. Similar to the SRP, the PCP comes into contact with the transparent acrylic pipe more frequently with longer external space constraints.

The flutter image sequence of the SRP and PCP with external space constraint is not displayed here anymore. However, a similar flutter image sequence can be found in (Ge et al., 2019).

The flutter critical flow velocity of the test pipe changes with the length of the external space constraint, as depicted in Fig. 19. As the length of the external space constraint increases, the flutter critical flow velocity generally increases. However, in some cases, the existing experimental conditions may not induce flutter instability in test pipe, such as when the external space constraint length is 1.0 m, as shown in Fig. 19(b). When the external space constraint length is short, like 0.2 and 0.4 m, the flutter critical flow velocity remains almost unchanged compared to the flutter critical flow velocity without an external space constraint (Config. 1a). Fig. 19 also illustrates the flutter critical flow velocity of the test pipe corresponding to the length of the unconstrained section under Config. 1a, represented by the green dashed line. For instance, in Fig. 19(a), when the length of the external space constraint is 1.2 m and the length of the unconstrained part for the SRP is 0.41 m, the flutter critical flow velocity of the SRP is 9.90 m/s, which is smaller than the flutter critical flow velocity of 12.25 m/s for the SRP with a length of 0.41 m under Config. 1a. The longer the external space constraint, the more restricted the movement of the SRP (or PCP) becomes, and the greater the flutter critical flow velocity, approaching that of the shorter SRP (or PCP) under Config. 1a.

4.4. Experiments without confinement immersed in water

In the experiment conducted under Config. 2a, 2<sup>#</sup> SRP and 3<sup>#</sup> PCP with the lengths indicated in Table 4 were used as test pipes. The other parameters remained the same as in Table 1. Water was poured into the tank until the water level reached 9 cm from the top, and the water inside the tank became completely static. The test pipe was then placed in the tank, and the pump frequency was gradually increased following to the experimental procedure. The flow velocity inside the pipe was gradually increased until the test pipe experienced flutter instability or the equipment approached the limit state, at which point the test was terminated. It is worth noting that all the test pipes experienced flutter instability under Config. 2a.

For the 2<sup>#</sup> SRP, the buckling phenomenon becomes more obvious before flutter as its length increases, as depicted in Fig. 20. At high flow velocities, such as 4.57 and 5.31 m/s, the 2<sup>#</sup> SRP even comes into contact with the tank wall. Buoyancy reduces the effective gravity of the 2<sup>#</sup> SRP, making it more flexible when it is longer. Consequently, when the flow velocity in the pipe is large, a complex flow field is formed in the tank, facilitating significant buckling of the 2<sup>#</sup> SRP and even causing it to touch the tank wall. On the other hand, when the 2<sup>#</sup> SRP is short, the buckling that occurs during the gradual increase of the flow velocity in the pipe is not as noticeable, as shown in Fig. 21.

The buckling phenomenon in the 3<sup>#</sup> PCP with two different lengths is not very pronounced as the flow velocity in the pipe gradually increases. Fig. 22 illustrates the buckling process of the 3<sup>#</sup>

**Table 3**  
Parameter combination of test pipes and confined space.

| Test pipes         |           | External space constraint         |                    |                    |
|--------------------|-----------|-----------------------------------|--------------------|--------------------|
| Type               | Length, m | Length, m                         | Inner diameter, mm | Outer diameter, mm |
| 2 <sup>#</sup> SRP | 1.61      | 0.2, 0.4, 0.6, 0.8, 1.0, 1.2, 1.4 | 24.98              | 45.47              |
| 3 <sup>#</sup> PCP | 1.61      | 0.2, 0.4, 0.6, 0.8, 1.0           | 24.98              | 45.47              |

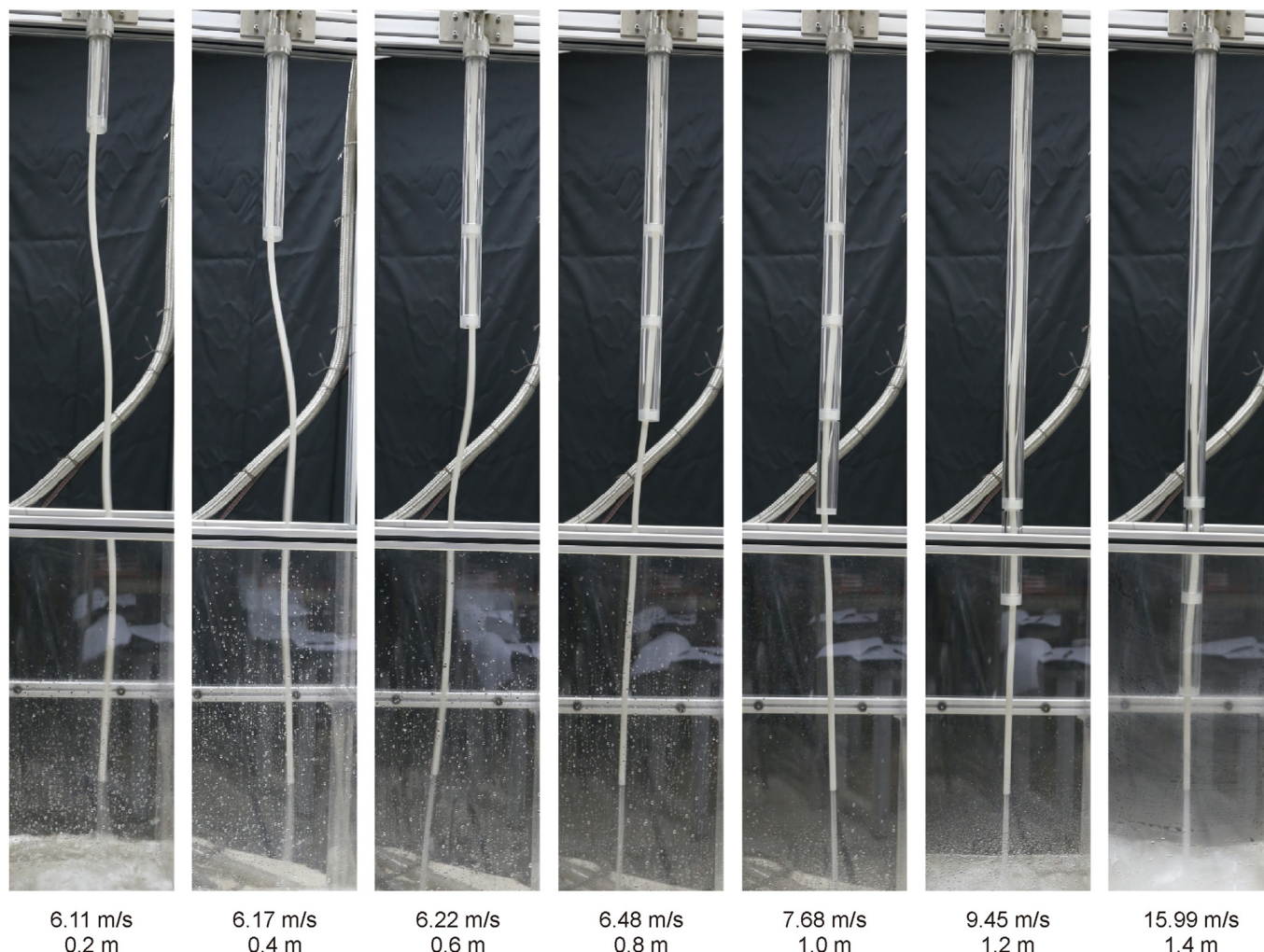


Fig. 17. Bending of the 2<sup>#</sup> SRP under different confined space length before flutter occurring in the air.

PCP with a length of 0.81 m. The shape of the 3<sup>#</sup> PCP with a length of 0.81 m undergoes slight changes before fluttering, and after flutter occurs, the PCP comes into contact with the tank wall and remains stationary.

The flutter critical flow velocity of the test pipe, immersed in water without external space constraint (under Config. 2a), is significantly smaller than that in the air without external space constraint (under Config. 1a), as shown in Fig. 23 and Table 5. For example, in Fig. 23, for all the 2<sup>#</sup> SRP with four lengths, the flutter critical flow velocity is significantly smaller than that under Config. 1a, and the change trend is basically the same. In other words, the larger the pipe length, the smaller the flutter critical flow velocity. However, due to the tank depth not being large enough, we were unable to observe the flutter critical flow velocity change trend of longer pipes. It should be noted that the 2<sup>#</sup> SRP with a length of 1.01 m touches the tank wall before fluttering. The flutter critical flow velocity obtained at this point is the flow velocity that causes the 2<sup>#</sup> SRP with a length of 1.01 m to move, which slightly distorts the result and makes it larger than the flutter critical flow velocity of the 2<sup>#</sup> SRP with a length of 0.81 m under Config. 2a. For 3<sup>#</sup> PCPs, the presence of surrounding water has a more significant impact on the flutter critical flow velocity. For instance, for the 3<sup>#</sup> PCP with a length of 0.81 m, we were unable to observe flutter instability

under Config. 1a due to equipment limitations. However, under Config. 2a, before reaching the equipment limit, flutter occurs with a critical flow velocity of 21.60 m/s. A similar phenomenon was also observed in the experiment conducted by Sugiyama et al. (1996), where they confirmed that the critical flutter velocity of the test pipe decreased with increasing immersed length of the lower end.

When the test pipe is immersed in water without any external space constraint (i.e. under Config. 2a), its motion observed to be different compared to that under Config. 1a. This difference is particularly noticeable especially when the SRP flutters, as depicted in Figs. 24 and 26. Fig. 24 illustrates the process of state change of the 2<sup>#</sup> SRP with  $L = 0.61$  m when it flutters under Config. 2a. When the 2<sup>#</sup> SRP with  $L = 0.61$  m flutters, it exhibits a motion where it swings on both sides and rotates in a certain direction. These two motions alternate with each other. However, the periodicity of this motion is slightly less apparent compared to its motion in the air (i.e., under Config. 1a) as shown in Fig. 25. Additionally, the overall state of motion in this case is more elegant.

Fig. 26 illustrates the process of the 3<sup>#</sup> PCP with  $L = 0.81$  m transitioning from a steady state to flutter instability under Config. 2a. Initially, the 3<sup>#</sup> PCP with  $L = 0.81$  m experiences slight vibrations. Over time, the swings of the 3<sup>#</sup> PCP with  $L = 0.81$  m become more pronounced until it makes contact with the tank wall and

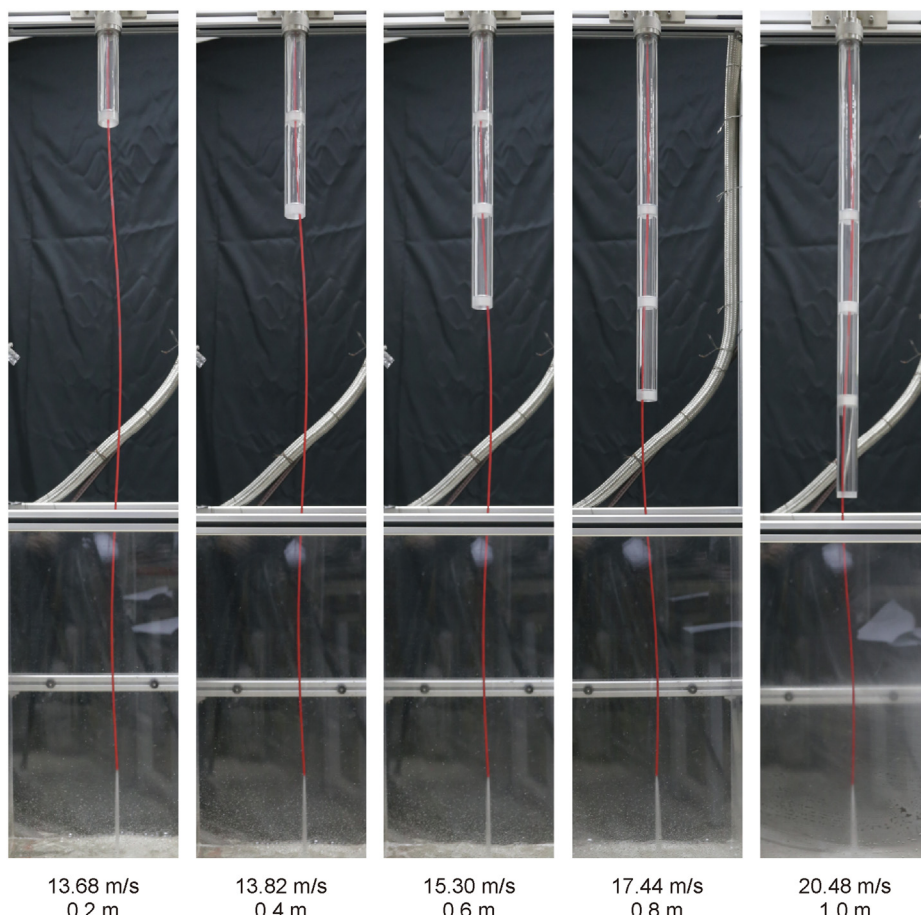


Fig. 18. Bending of the 3<sup>#</sup> PCP under different confined space length before flutter occurring in the air.

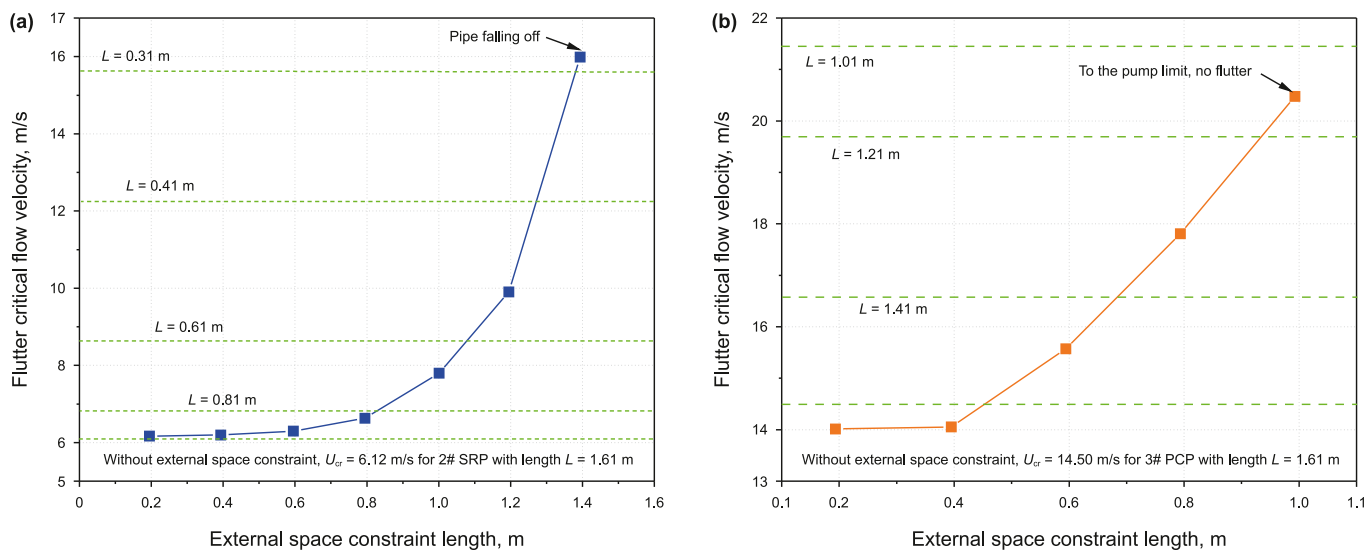


Fig. 19. Flutter critical flow velocity under Config. 1b versus the length of external space constraint, (a) 2<sup>#</sup> SRP, (b) 3<sup>#</sup> PCP.

comes to a stop, as shown in the final state in Fig. 22. However, under Config. 1a, where there are no external space constraints in the air, the 3<sup>#</sup> PCP with  $L = 1.01$  m does not touch the tank wall during flutter.

#### 4.5. Experiments with confinement immersed in water

In the experiment conducted under Config. 2b, a transparent acrylic pipe was used as an external space constraint, as depicted in

**Table 4**  
Geometric parameters of test pipes immersed in water without external space constraint.

| Test pipes         | Length, m              |
|--------------------|------------------------|
| 2 <sup>#</sup> SRP | 0.41, 0.61, 0.81, 1.01 |
| 3 <sup>#</sup> PCP | 0.81, 1.01             |

Fig. 16. The test pipes utilized were 2<sup>#</sup> SRP and 3<sup>#</sup> PCP, with the test pipe partially confined within the transparent acrylic pipe. The length combinations of the test pipes and external space constraint under Config. 2b are summarized in Table 6, while the other parameters remain the same as those Table 1. During the experiment, the test pipe with the external space constraint was submerged in water, and the pump frequency was gradually increased following the test procedure outlined in Section 4. Consequently, the flow velocity within the pipe gradually increased. The experiment was concluded either when the test pipe experienced flutter instability or when the equipment approached its limit state. It is worth noting that, under the test conditions of Config. 2b, all the test pipes exhibited flutter instability, except for 3<sup>#</sup> PCP with a 0.6 m external space constraint.

The SRP buckled as the flow velocity gradually increased during the experiment conducted under the length constraint of external

space specified in Config. 2b. Initially, the SRP was not in contact with the transparent acrylic pipe, but it eventually buckled and made contact. Fig. 27 illustrates the buckling state of a 2<sup>#</sup> SRP immersed in water at a higher flow velocity before flutter, with different lengths of external space constraint. In the case where the external space constraint is 0.2 m and the unconstrained part of the SRP is 0.8 m, the flow velocity inside the SRP of 4.53 m/s causes it to come into contact with the tank wall due to a greater degree of bending. This situation is similar to the last two states shown in Fig. 20. When the external space constraint length was shorter, meaning the ratio of the external space constraint length to the cantilevered pipe length is smaller, such as 0.2 m, the buckling state of the unconstrained part of the SRP resembled the buckling state observed under Config. 2a (shown in Fig. 20). On the other hand, when the external space constraint length was longer, for example, 0.8 m, the buckling of the SRP was restricted by the annular space, resulting in a lesser likelihood of buckling in the unconstrained part of the SRP. However, the unconstrained part of the SRP appears straighter in this case.

In the experiment under Config. 2b, the PCP was not in contact with the transparent acrylic pipe until it buckled and came into contact with it, except for the 0.2 m external space constraint. Fig. 28 shows the buckling state of a 3<sup>#</sup> PCP immersed in water with different lengths of external space constraint at a higher flow velocity before flutter. Similar to the SRP, the longer the external space

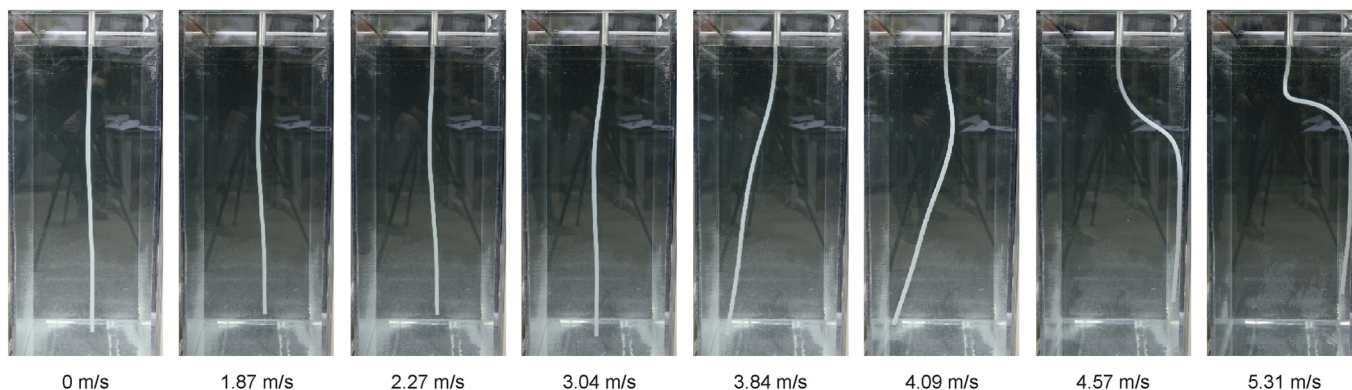


Fig. 20. Bending of a 2<sup>#</sup> SRP with  $L = 1.01$  m immersed in water without confined space before flutter occurring.

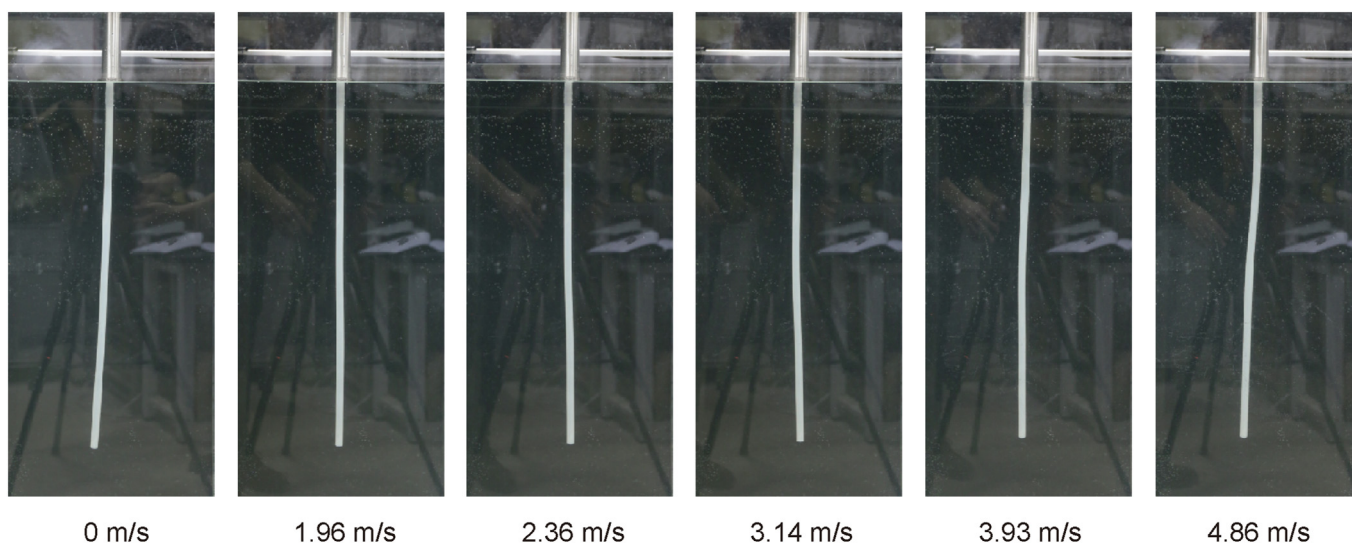


Fig. 21. Bending of a 2<sup>#</sup> SRP with  $L = 0.61$  m immersed in water without confined space before flutter occurring.

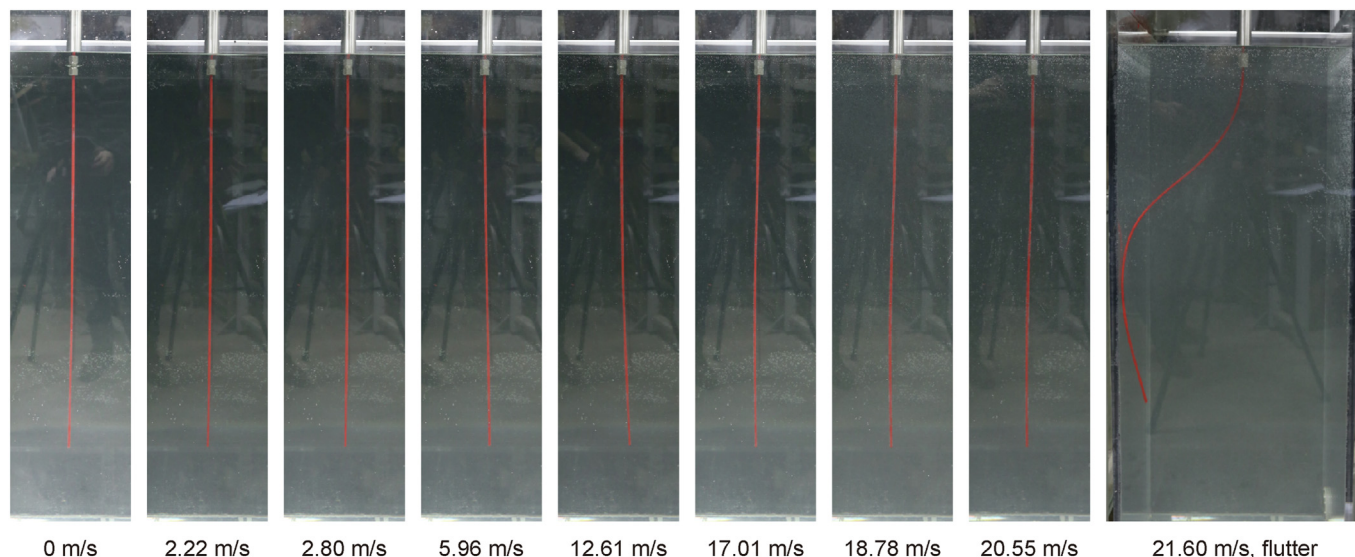


Fig. 22. Bending of a 3<sup>#</sup> PCP with  $L = 0.81$  m immersed in water without confined space before flutter occurring.

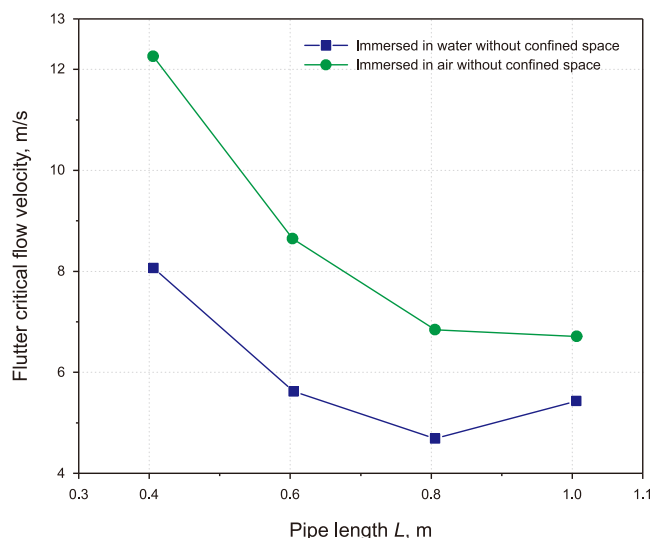


Fig. 23. Flutter critical flow velocity of 2<sup>#</sup> SRPs immersed in water without confined space versus the pipe length.

constraint, the more the PCP comes into contact with the annular space, making it more difficult for the unconstrained part of the PCP to buckle.

The flutter critical flow velocity of the test pipe under Config. 2b changes with the length of the external space constraint, as depicted in Fig. 29. In general, the flutter critical flow velocity increases as the length of the external space constraint increases. Even under the existing experimental conditions, the test pipe cannot be destabilized, as shown in Fig. 29(b). In the case of the 2<sup>#</sup> SRP with a length of 1.01 m (Fig. 29(a)), when the external space constraint length is short (e.g., 0.2 and 0.4 m), the SRP has fewer contact points with the surrounding tube. Consequently, the flutter critical flow velocity hardly changes with the length of the confined space, which aligns with the flutter critical flow velocity of the 2<sup>#</sup> SRP without an external space constraint. For the 3<sup>#</sup> PCP with a length of 1.01 m (Fig. 29(b)), when the external space constraint length is 0.2 and 0.4 m respectively, the former never contacts the PCP, while the latter does, resulting in a larger flutter critical flow velocity. When the external space constraint length is 0.6 m, the PCP does not experience flutter instability before the equipment reaching its limit. Overall, the longer the external space constraint,

Table 5

Flutter critical flow velocity of 3<sup>#</sup> PCPs immersed in water without confined space versus the pipe length.

| Pipe length, m | In water without confinement | In air without confinement                          |
|----------------|------------------------------|---|
| 1.01           | 17.09                        | 21.45   |
| 0.81           | 21.60                        | Failed to flutter under the experimental conditions |

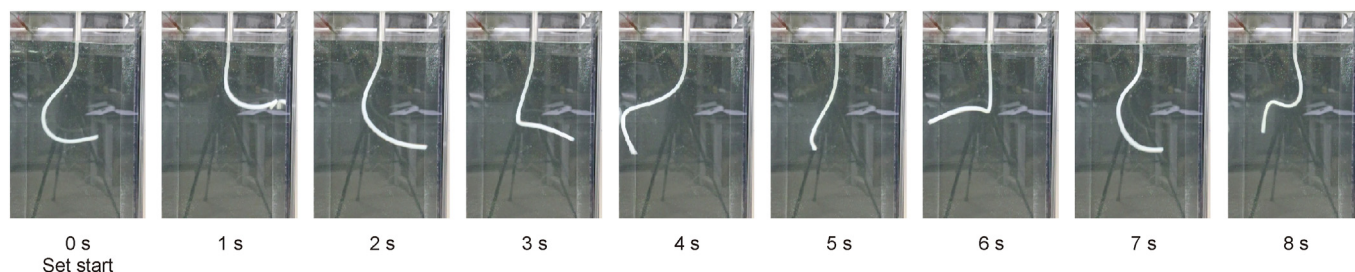


Fig. 24. Flutter process of a 2<sup>#</sup> SRP with  $L = 0.61$  m immersed in water without confined space.

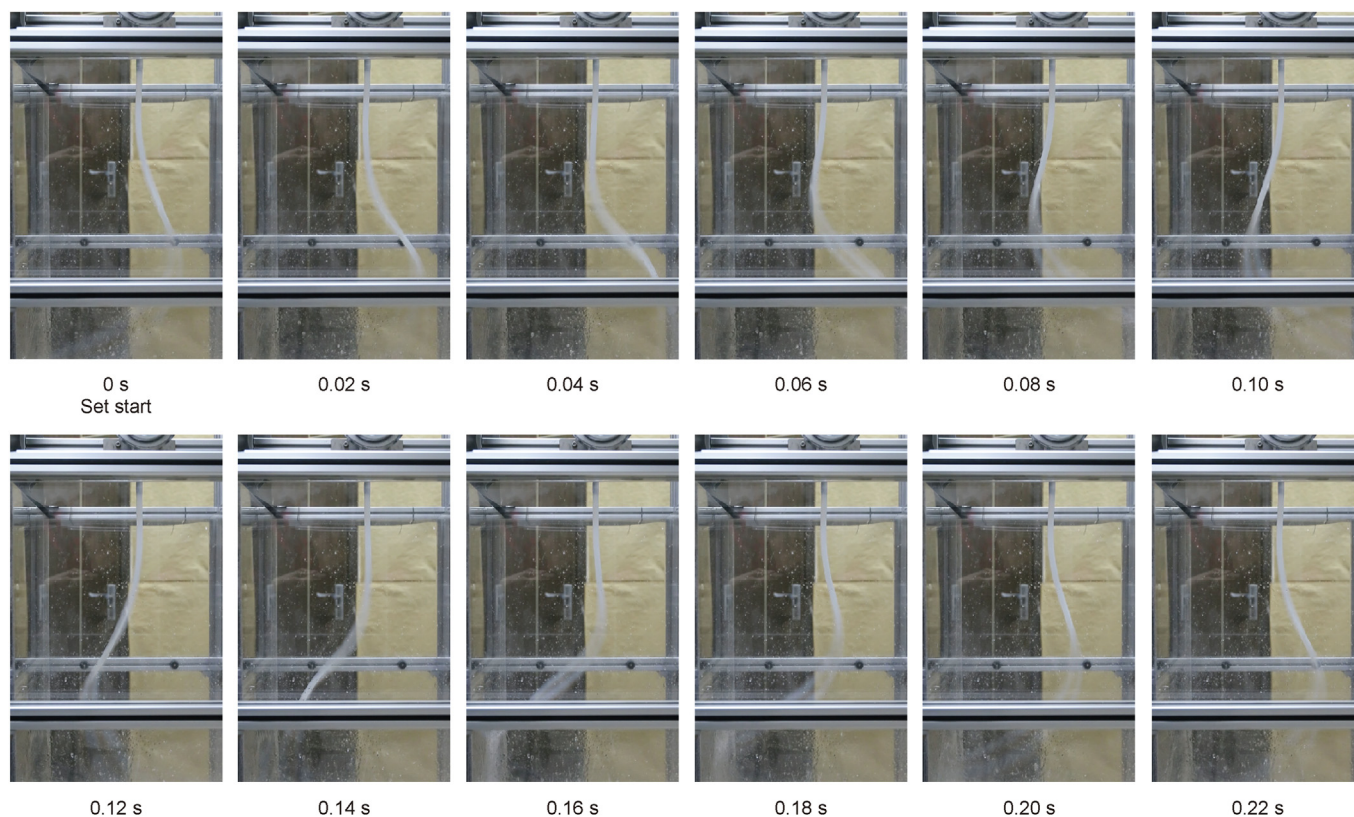


Fig. 25. Flutter process of a 2<sup>#</sup> SRP with  $L = 0.61$  m in air without confined space.

the more restrictive the test pipe becomes, leading to a higher flutter critical flow velocity in this state. It approaches the flutter critical flow velocity of the test pipe with the corresponding remaining length under Config. 2a. The presence of external space constraints leads to a reduction in the effective length of the pipe, resulting in an increase in added mass and inertia. Consequently, the flutter critical flow velocity increases with the length of the external space constraint (Fig. 29).

When the test pipe flutters under Config. 2b, its motion is of interest. For the 2<sup>#</sup> SRP, when the external space constraint length is 0.2, 0.4, and 0.6 m respectively, the motion of the pipe during flutter is similar to that shown in Fig. 24. The movement posture appears to be elegant and changeable. When the external space constraint length is 0.8 m, the unconstrained part of the SRP is shorter. During flutter, the SRP swings and changes the swing plane alternately, and the frequency is faster. Fig. 30 shows the motion of the 2<sup>#</sup> SRP in a swing plane within one period. Compared with the movement in the air, the pipe is more prone to bending.

When the external space constraint length is 0.2 and 0.4 m, respectively, the motion of the pipe is similar during the 3<sup>#</sup> PCP fluttering in both cases. Fig. 31 illustrates the motion of the PCP with an external space constraint of 0.2 m during fluttering. The PCP moves periodically in a certain direction (counterclockwise from top to bottom), at a slower frequency. Additionally, due to the large movement range, the PCP comes into contact with the tank wall, which is similar to the motion of the PCP with lengths of 1.01 and 0.81 m under Config. 2a during fluttering.

## 5. Summary and conclusion

In this paper, the dynamics of leaching tubing in a laboratory apparatus are investigated using SRPs and PCPs. The experiments were conducted under six configurations (shown in Fig. 6), including pipes totally immersed in air, pipes with an external space constraint totally immersed in air, pipes totally immersed in water, pipes with an external space constraint totally immersed in water, and pipes with a Y-shaped or T-shaped end. The experimental results reveal several dynamic response phenomena, namely, water hammer, static buckling, chaotic motion, and flutter instability. It has been confirmed that most test pipes will experience flutter instability at sufficiently high flow velocities. The effects of parameters such as external space constraint, flexural rigidity, medium outside the pipe, overhanging length of the pipe and end conditions on the flutter critical flow velocity are studied experimentally. The main conclusions and proposals are as follows:

- (1) The presence of a penpoint-like end has little effect on the flutter critical flow velocity of the cantilevered pipe conveying fluid. The flutter critical flow velocity for a test pipe with the penpoint-like end is almost the same as that for a test pipe without the penpoint-like end.
- (2) Experimental results indicate that the inverted Y-type end and the inverted T-type end can increase the flutter critical flow velocity, with the inverted T-type end having a more significant effect. The inverted Y-type end leads to a greater degree of buckling in the SRP, while the inverted T-type end can stabilize the SRP without causing the cantilevered pipe to buckle. Therefore, during cavern leaching, an inverted T-type

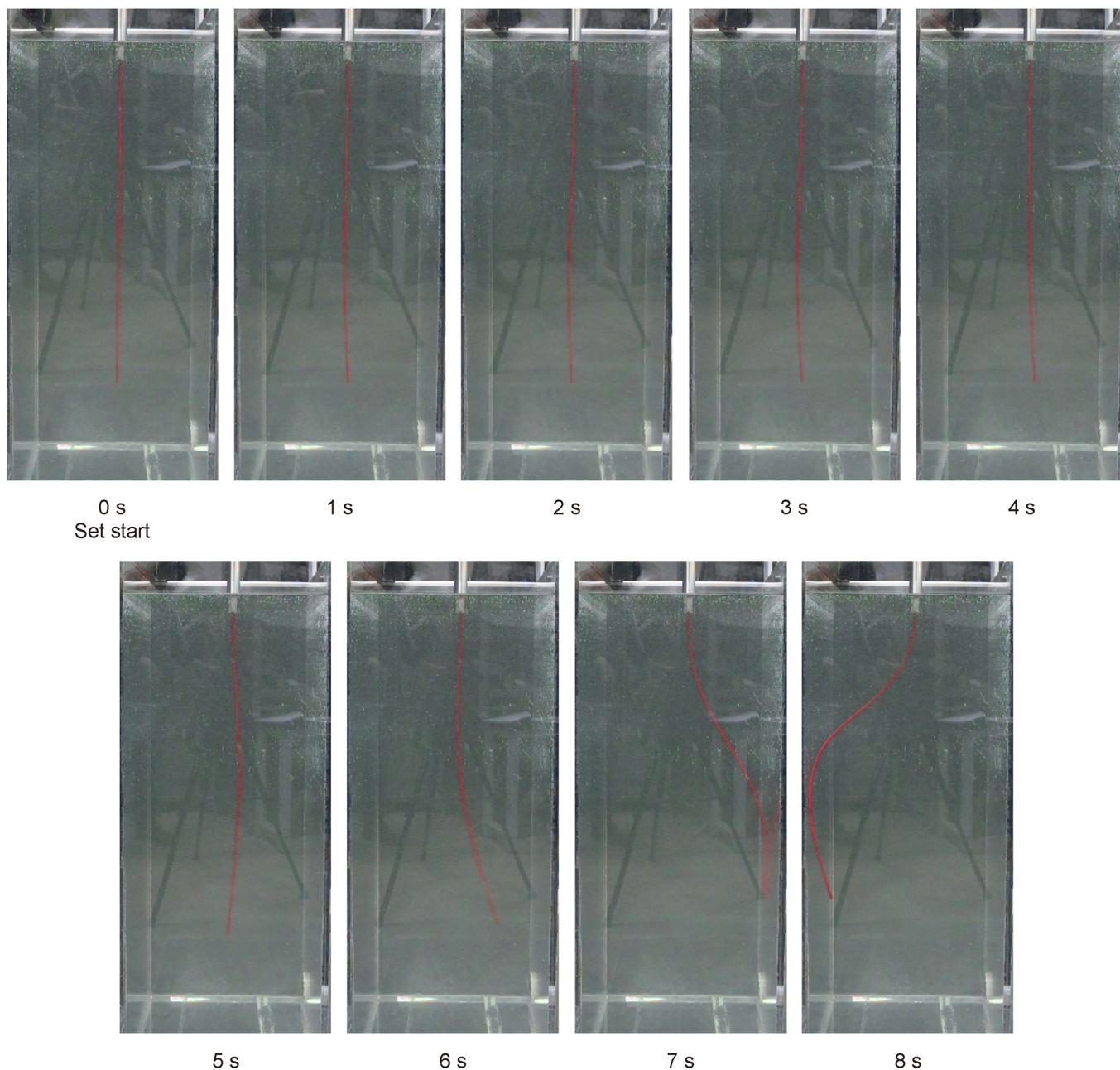


Fig. 26. Amplitude increasing process of a 2<sup>#</sup> PCP with  $L = 0.81$  m immersed in water without confined space.

**Table 6**  
Parameter combination of test pipes immersed in water and confined space.

| Test pipes         | Length of external space constraint, m |                         |
|--------------------|--|-------------------------|
| Type               | Length, m                              |                         |
| 2 <sup>#</sup> SRP | 1.01                                   | 0.2, 0.4, 0.6, 0.8, 1.0 |
| 3 <sup>#</sup> PCP | 1.01                                   | 0.2, 0.4, 0.6           |

end or inverted Y-type end can be utilized to prevent flutter instability of the leaching tubing, but it is important to prevent uneven bifurcation of the water flow at the end.

(3) The buckling of the test pipe can be restrained by the external space constraint, whether it is in the air or

underwater. Moreover, the longer the external space constraint, the more limited the movement of the test pipe becomes, resulting in a higher the flutter critical flow velocity. This velocity is also closer to the flutter critical flow

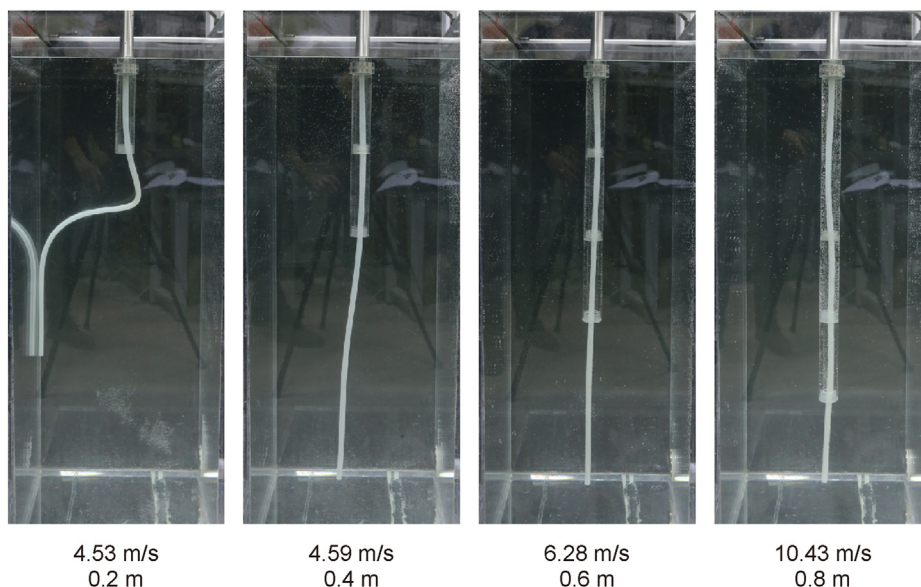


Fig. 27. Bending of a 2<sup>#</sup> SRP immersed in water under different confined space length before flutter occurring.

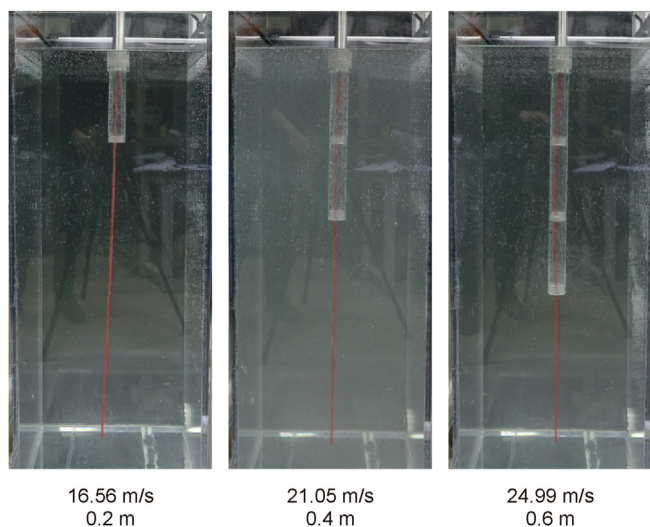


Fig. 28. Bending of a 3<sup>#</sup> SRP immersed in water under different confined space length before flutter occurring.

velocity of the unconstrained test pipe under Config. 1a or Config. 2a.

- (4) When the test pipe is immersed in water without the external space constraint, the flutter critical flow velocity is significantly lower compared to when it is in the air without any constraint.

**CRedit authorship contribution statement**

**Yin-Ping Li:** Resources, Methodology, Conceptualization. **Xin-Bo Ge:** Writing – review & editing, Writing – original draft, Visualization, Validation, Data curation. **Xi-Lin Shi:** Supervision, Software, Funding acquisition. **Hong-Ling Ma:** Writing – review & editing, Supervision, Investigation.

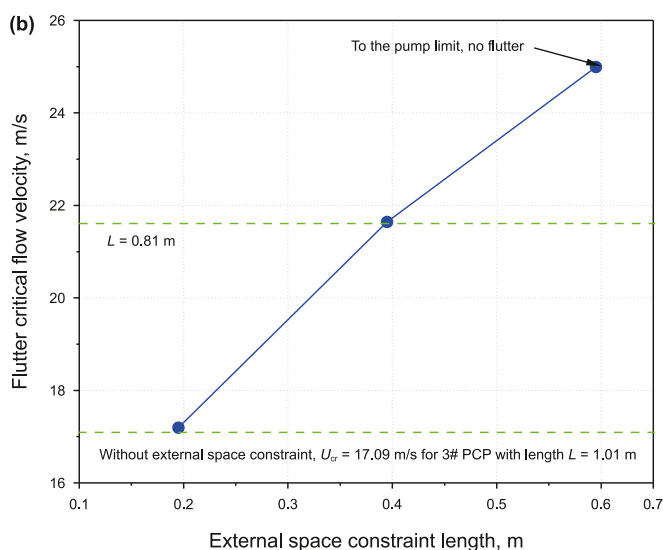
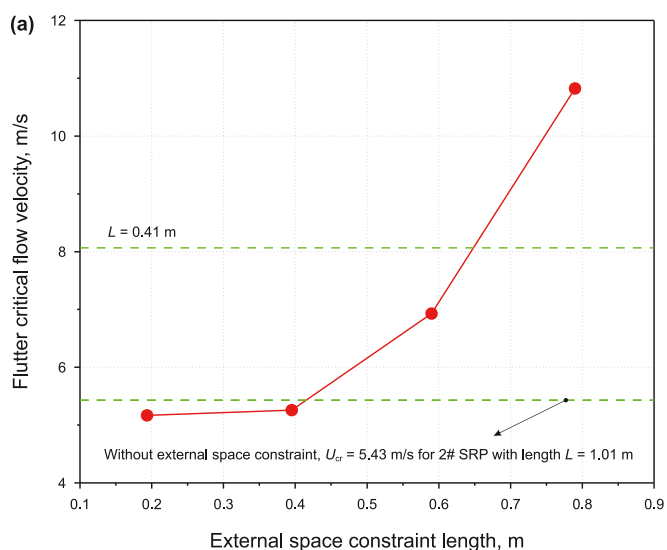


Fig. 29. Flutter critical flow velocity under Config. 2b versus the length of external space constraint, (a) for 2<sup>#</sup> SRP, (b) for 3<sup>#</sup> PCP.

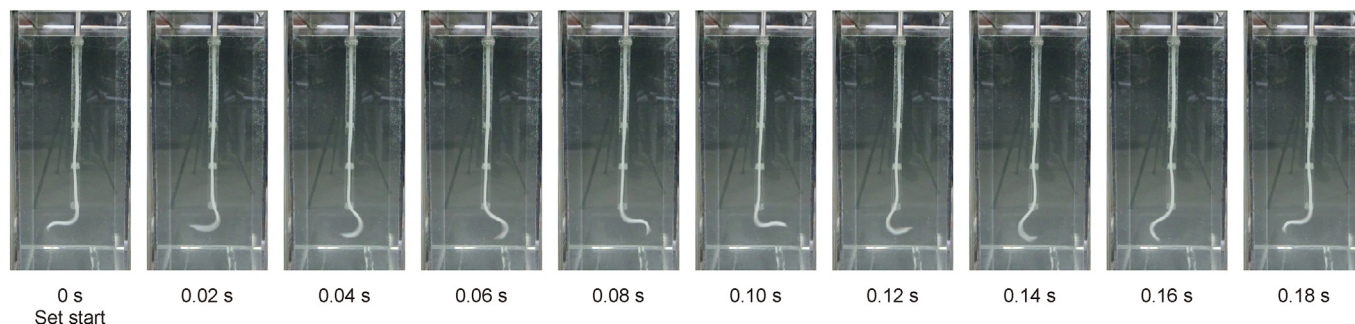


Fig. 30. Flutter process of a 2<sup>#</sup> SRP with  $L = 1.01$  m immersed in water with confined space length 0.8 m.

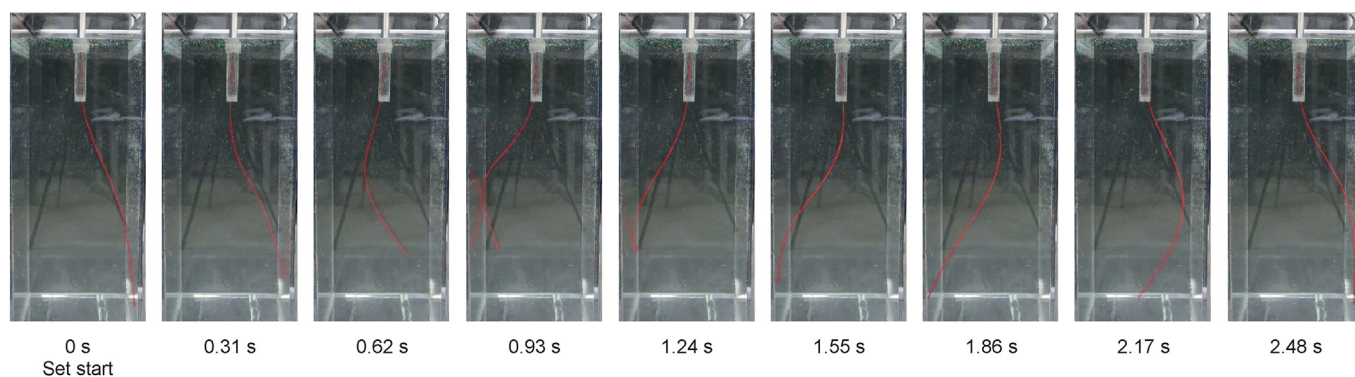


Fig. 31. Flutter process of a 3<sup>#</sup> PCP with  $L = 1.01$  m immersed in water with confined space length 0.2 m.

**Declaration of interest statement**

We declare that we have no financial and personal relationships with other people or organizations that can inappropriately influ-

**Nomenclature**

| Nomenclature |   |                   |              |  |                  |
|--------------|---|-------------------|--------------|--|------------------|
| $d$          | inner diameter of the pipe                | m                 | $u$          | non-dimensional flutter critical flow velocity | –                |
| $D$          | outer diameter of the pipe                | m                 | $U$          | flow velocity in the pipe                      | $m \cdot s^{-1}$ |
| $EI$         | flexural rigidity                         | $N \cdot m^2$     | $X$          | longitudinal coordinate                        | m                |
| $g$          | gravity                                   | m                 | $Y$          | lateral deflection of the pipe                 | m                |
| $L$          | length of pipe                            | m                 | Greek symbol |  |                  |
| $m$          | mass of the pipe per unit length          | $kg \cdot m^{-1}$ | $\beta$      | non-dimensional mass ratio                     | –                |
| $M$          | mass of water in the pipe per unit length | $kg \cdot m^{-1}$ | $\gamma$     | non-dimensional gravity                        | –                |
| $t$          | time                                      | s                 |              |  |                  |

ence our work, there is no professional or other personal interest of any nature or kind in any product, service and/or company that could be construed as influencing the position presented in, or the review of, the manuscript entitled.

**Acknowledgements**

The authors gratefully acknowledge the financial support received from the Open Research Fund of the State Key Laboratory of Geomechanics and Geotechnical Engineering, Institute of Rock and Soil Mechanics, Chinese Academy of Sciences (Grant No. Z019011), the Shandong Provincial Natural Science Foundation (Grant No. ZR2020QE112), the National Natural Science Foundation of China (No. 51874273) and the Excellent Young Scientists Fund Program of National Natural Science Foundation of China (No. 52122403).

**References**

Askarian, A.R., Rahmanian, M., Haddadpour, H., et al., 2020. Bending-torsional stability analysis of aerodynamically covered pipes with inclined terminal nozzle and concurrent internal and external flows. *J. Fluid Struct.* 94, 102932. <https://doi.org/10.1016/j.jfluidstructs.2020.102932>.

Brouard, B., Bérest, P., Couateau, J., 1997. Influence of the leaching phase on the mechanical behavior of salt caverns. *Int. J. Rock Mech. Min. Sci.* 34 (3–4), 26.e1–26.e15. [https://doi.org/10.1016/S1365-1609\(97\)00019-1](https://doi.org/10.1016/S1365-1609(97)00019-1).

Chen, J., Lu, D., Liu, W., et al., 2020a. Stability study and optimization design of small-spacing two-well (SSTW) salt caverns for natural gas storages. *J. Energy Storage* 27, 101131. <https://doi.org/10.1016/j.est.2019.101131>.

Chen, J., Peng, H.H., Fan, J.Y., et al., 2020b. Microscopic investigations on the healing and softening of damaged salt by uniaxial deformation from CT, SEM and NMR: effect of fluids (brine and oil). *RSC Adv.* 10 (5), 2877–2886. <https://doi.org/10.1039/C9RA05866D>.

Chen, X.S., Li, Y.P., Jiang, Y.L., et al., 2022. Theoretical research on gas seepage in the formations surrounding bedded gas storage salt cavern. *Petrol. Sci.* 19 (4), 1766–1778. <https://doi.org/10.1016/j.petsci.2022.01.021>.

Chen, X.S., Li, Y.P., Shi, Y.F., et al., 2021. Tightness and stability evaluation of salt

- cavern underground storage with a new fluid-solid coupling seepage model. *J. Pet. Sci. Eng.* 202, 108475. <https://doi.org/10.1016/j.petrol.2021.108475>.
- da Costa, A., Amaral, C., Poiate, E., et al., 2011. Underground Storage of Natural Gas and CO<sub>2</sub> in Salt Caverns in Deep and Ultra-deep Water Offshore Brazil. 12th ISRM Congress. International Society for Rock Mechanics, Beijing, China. October 2011.
- Doaré, O., De Langre, E., 2002. The flow-induced instability of long hanging pipes. *Eur. J. Mech. Solid.* 21 (5), 857–867. [https://doi.org/10.1016/S0997-7538\(02\)01221-4](https://doi.org/10.1016/S0997-7538(02)01221-4).
- Edelstein, W.S., Chen, S.S., 1985. Flow-induced instability of an elastic tube with a variable support. *Nucl. Eng. Des.* 84 (1), 1–11. [https://doi.org/10.1016/0029-5493\(85\)90308-5](https://doi.org/10.1016/0029-5493(85)90308-5).
- Evans, D.J., Chadwick, R., 2009. *Underground Gas Storage: Worldwide Experiences and Future Development in the UK and Europe*. Geological Society Special Publication, London.
- Fan, H.H., Li, C.W., Wang, Z.M., et al., 2017. Dynamic analysis of a hang-off drilling riser considering internal solitary wave and vessel motion. *J. Nat. Gas Sci. Eng.* 37, 512–522. <https://doi.org/10.1016/j.jngse.2016.12.003>.
- Feng, Y., Xiao, X.M., Wang, E.Z., et al., 2023. Gas storage in shale pore system: a review of the mechanism, control and assessment. *Petrol. Sci.* 20 (5), 2605–2636. <https://doi.org/10.1016/j.petsci.2023.05.012>.
- Firme, P.A.L.P., Roehl, D., Romanel, C., 2019. Salt caverns history and geomechanics towards future natural gas strategic storage in Brazil. *J. Nat. Gas Sci. Eng.* 72, 103006. <https://doi.org/10.1016/j.jngse.2019.103006>.
- Fireouz-Abadi, R.D., Askarian, A.R., Kheiri, M., 2013. Bending–torsional flutter of a cantilevered pipe conveying fluid with an inclined terminal nozzle. *J. Sound Vib.* 332 (12), 3002–3014. <https://doi.org/10.1016/j.jsv.2012.12.038>.
- Ge, X.B., Li, Y.P., Shi, X.L., et al., 2019. Experimental device for the study of liquid–solid coupled flutter instability of salt cavern leaching tubing. *J. Nat. Gas Sci. Eng.* 66, 168–179. <https://doi.org/10.1016/j.jngse.2019.03.026>.
- Ge, X.B., Li, Y.P., Shi, X.L., et al., 2021. Dynamics and enhanced stability properties of slender leaching tubings in salt cavern storage with a Y-type manifold fitted at free downstream end. *J. Energy Storage.* 43, 103170. <https://doi.org/10.1016/j.est.2021.103170>.
- Han, Y., Ma, H.L., Yang, C.H., et al., 2021. The mechanical behavior of rock salt under different confining pressure unloading rates during compressed air energy storage (CAES). *J. Pet. Sci. Eng.* 196, 107676. <https://doi.org/10.1016/j.petrol.2020.107676>.
- Hannoyer, M.J., Paidoussis, M.P., 1979a. Dynamics of slender tapered beams with internal or external axial-flow, Part 2: experiments. *J. Appl. Mech. ASME* 46 (1), 52–57. <https://doi.org/10.1115/1.3424527>.
- Hannoyer, M.J., Paidoussis, M.P., 1979b. Dynamics of slender tapered beams with internal or external axial flow, Part 1: theory. *J. Appl. Mech.* 46 (1), 45–51. <https://doi.org/10.1115/1.3424526>.
- Ibrahim, R.A., 2010. Overview of mechanics of pipes conveying fluids-part I: fundamental studies. *J. Press. Vess. ASME* 132 (3), 034001. <https://doi.org/10.1115/1.4001271>.
- Ibrahim, R.A., 2011. Mechanics of pipes conveying fluids—part II: applications and fluidelastic problems. *J. Pressure Vessel Technol.* 133 (2), 024001. <https://doi.org/10.1115/1.4001270>.
- Jendrzeczyk, J.A., Chen, S.S., 1985. Experiments on tubes conveying fluid. *Thin-Walled Struct.* 3 (2), 109–134. [https://doi.org/10.1016/0263-8231\(85\)90028-x](https://doi.org/10.1016/0263-8231(85)90028-x).
- Khudayarov, B.A., Komilova, K.M., Turaev, F.Z., 2020. Dynamic analysis of the suspended composite pipelines conveying pulsating fluid. *J. Nat. Gas Sci. Eng.* 75, 103148. <https://doi.org/10.1016/j.jngse.2020.103148>.
- Kuiper, G., Metrikine, A., 2008. Experimental investigation of dynamic stability of a cantilever pipe aspirating fluid. *J. Fluid Struct.* 24 (4), 541–558. <https://doi.org/10.1016/j.jfluidstructs.2007.10.011>.
- Li, J.L., Tang, Y., Shi, X.L., et al., 2019. Modeling the construction of energy storage salt caverns in bedded salt. *Appl. Energy* 255, 113866. <https://doi.org/10.1016/j.apenergy.2019.113866>.
- Li, J.L., Xu, W.J., Zheng, J.J., et al., 2020. Modeling the mining of energy storage salt caverns using a structural dynamic mesh. *Energy* 193, 116730. <https://doi.org/10.1016/j.energy.2019.116730>.
- Li, Y., Ge, X., Wang, B., et al., 2016a. Preliminary Investigation of Dynamic Characteristics of Leaching Strings for Solution Mining of Salt Cavern Storage. 50th US Rock Mechanics/Geomechanics Symposium 2016, June 26–29. American Rock Mechanics Association (ARMA), Houston, TX, United States, pp. 531–536.
- Li, Y.P., Ge, X.B., Wang, B.W., et al., 2016b. Dynamic stability tests on tubing string for solution mining of a salt cavern UGS. *Nat. Gas. Ind.* 36 (7), 81–87. <https://doi.org/10.3787/j.issn.1000-0976.2016.07.012>.
- Liu, W., Zhang, X., Fan, J.Y., et al., 2020. Evaluation of potential for salt cavern gas storage and integration of brine extraction: cavern utilization, yangtze river delta region. *Nat. Resour. Res.* 29, 3275–3290. <https://doi.org/10.1007/s11053-020-09640-4>.
- Lundgren, T., Sethna, P., Bajaj, A., 1979. Stability boundaries for flow induced motions of tubes with an inclined terminal nozzle. *J. Sound Vib.* 64 (4), 553–571. [https://doi.org/10.1016/0022-460X\(79\)90804-6](https://doi.org/10.1016/0022-460X(79)90804-6).
- Mao, L.J., Liu, Q.Y., Zhou, S.W., et al., 2016. Deep water drilling riser mechanical behavior analysis considering actual riser string configuration. *J. Nat. Gas Sci. Eng.* 33, 240–254. <https://doi.org/10.1016/j.jngse.2016.05.031>.
- Modarres-Sadeghi, Y., Semler, C., Wadham-Gagnon, M., et al., 2007. Dynamics of cantilevered pipes conveying fluid. Part 3: three-dimensional dynamics in the presence of an end-mass. *J. Fluid Struct.* 23 (4), 589–603. <https://doi.org/10.1016/j.jfluidstructs.2006.10.007>.
- Moditis, K., Paidoussis, M.P., Ratigan, J., 2016. Dynamics of a partially confined, discharging, cantilever pipe with reverse external flow. *J. Fluid Struct.* 63, 120–139. <https://doi.org/10.1016/j.jfluidstructs.2016.03.002>.
- Ozarslan, A., 2012. Large-scale hydrogen energy storage in salt caverns. *Int. J. Hydrogen Energy* 37 (19), 14265–14277. <https://doi.org/10.1016/j.ijhydene.2012.07.111>.
- Paidoussis, M.P., 1970. Dynamics of tubular cantilevers conveying fluid. *Proc. Inst. Mech. Eng. Part C J. Mech. Eng. Sci.* 12 (2), 85–103. [https://doi.org/10.1243/JMES\\_JOUR\\_1970\\_012\\_017\\_02](https://doi.org/10.1243/JMES_JOUR_1970_012_017_02).
- Paidoussis, M.P., 2014. Vol. 1 second ed. *Fluid-structure Interactions: Slender Structures and Axial Flow*. Academic press, Oxford, UK.
- Paidoussis, M.P., 2022. Pipes conveying fluid: a fertile dynamics problem. *J. Fluid Struct.* 114, 103664. <https://doi.org/10.1016/j.jfluidstructs.2022.103664>.
- Paidoussis, M.P., Abdelbaki, A.R., Butt, M.F.J., et al., 2021. Dynamics of a cantilevered pipe subjected to internal and reverse external axial flow: a review. *J. Fluid Struct.* 106, 103349. <https://doi.org/10.1016/j.jfluidstructs.2021.103349>.
- Pettigrew, M., Paidoussis, M., 1975. Dynamics and stability of flexible cylinders subjected to liquid and two-phase axial flow in confined annuli. In: *Third International Conference on Structural Mechanics in Reactor Technology*. U.K., London.
- Rinaldi, S., Paidoussis, M.P., 2010. Dynamics of a cantilevered pipe discharging fluid, fitted with a stabilizing end-piece. *J. Fluid Struct.* 26 (3), 517–525. <https://doi.org/10.1016/j.jfluidstructs.2010.01.004>.
- Shaaban, A., Chehreghani, M., Misra, A.K., et al., 2023. The dynamics of imperfectly supported hanging pipes conveying fluid: an experimental study. *J. Fluid Struct.* 121, 103951. <https://doi.org/10.1016/j.jfluidstructs.2023.103951>.
- Shahmorad, Z., Salarirad, H., Molladavoudi, H., 2016. A study on the effect of utilizing different constitutive models in the stability analysis of an underground gas storage within a salt structure. *J. Nat. Gas Sci. Eng.* 33, 808–820. <https://doi.org/10.1016/j.jngse.2016.06.011>.
- Shi, X.L., Li, Y.P., Yang, C.H., et al., 2015. Influences of filling abandoned salt caverns with alkali wastes on surface subsidence. *Environ. Earth Sci.* 73 (11), 6939–6950. <https://doi.org/10.1007/s12665-015-4135-y>.
- Shi, X.L., Wei, X.X., Yang, C.H., et al., 2023. Problems and countermeasures for construction of China's salt cavern type strategic oil storage. *Bull. Chin. Acad. Sci.* 38 (1), 99–111. <https://doi.org/10.16418/j.issn.1000-3045.20221014005>.
- Sugiyama, Y., Katayama, T., Kanki, E., et al., 1996. Stability of vertical fluid-conveying pipes having the lower end immersed in fluid. *JSME Int. J., Ser. B.* 39 (1), 57–65. <https://doi.org/10.1299/jsmeb.39.57>.
- Sun, W., Li, M.Y., Liu, Y.D., et al., 2023. Study of main factors influencing unsteady-state temperature drop in oil tank storage under dynamic thermal environment coupling. *Petrol. Sci.* 20 (6), 3783–3797. <https://doi.org/10.1016/j.petsci.2023.08.003>.
- Wang, L., Dai, H.L., 2012. Vibration and enhanced stability properties of fluid-conveying pipes with two symmetric elbows fitted at downstream end. *Arch. Appl. Mech.* 82 (2), 155–161. <https://doi.org/10.1007/s00419-011-0545-9>.
- Wang, T.T., Li, J.J., Jing, G., et al., 2019. Determination of the maximum allowable gas pressure for an underground gas storage salt cavern—a case study of Jintan, China. *J. Rock Mech. Geotech. Eng.* 11 (2), 251–262. <https://doi.org/10.1016/j.jrmge.2018.10.004>.
- Wang, T.T., Ma, H.L., Shi, X.L., et al., 2018a. Salt cavern gas storage in an ultra-deep formation in Hubei, China. *Int. J. Rock Mech. Min. Sci.* 102, 57–70. <https://doi.org/10.1016/j.ijrmms.2017.12.001>.
- Wang, T.T., Yang, C.H., Chen, J.S., et al., 2018b. Geomechanical investigation of roof failure of China's first gas storage salt cavern. *Eng. Geol.* 243, 59–69. <https://doi.org/10.1016/j.enggeo.2018.06.013>.
- Wang, Y.B., Gao, D.L., Fang, J., 2014. Static analysis of deep-water marine riser subjected to both axial and lateral forces in its installation. *J. Nat. Gas Sci. Eng.* 19, 84–90. <https://doi.org/10.1016/j.jngse.2014.04.019>.
- Xu, J., Huang, Y.Y., 2000. Bifurcations of a cantilevered pipe conveying steady fluid with a terminal nozzle. *Acta Mech. Sin.* 16 (3), 264–272. <https://doi.org/10.1007/BF02487667>.
- Yang, C.H., Wang, T.T., Chen, H.S., 2023. Theoretical and technological challenges of deep underground energy storage in China. *Engineering* 25, 168–181. <https://doi.org/10.1016/j.eng.2022.06.021>.
- Yoshizawa, M., Suzuki, T., Takayanagi, M., et al., 1998. Nonlinear lateral vibration of a vertical fluid-conveying pipe with end mass. *JSME Int. J., Ser. C.* 41 (3), 652–661. <https://doi.org/10.1299/jsmecc.41.652>.
- Zhang, G.M., Li, Y.P., Yang, C.H., et al., 2014. Stability and tightness evaluation of bedded rock salt formations for underground gas/oil storage. *Acta Geotech* 9 (1), 161–179. <https://doi.org/10.1007/s11440-013-0227-6>.